Icarus 358 (2021) 114275

Contents lists available at ScienceDirect

Icarus

journal homepage: www.elsevier.com/locate/icarus

Research Paper

The orbit of asteroid (317) Roxane's satellite Olympias from Gemini, Keck, VLT and the SOR, and (22) Kalliope's Linus from the SOR

Jack D. Drummond [a,*], W.J. Merline [b], B. Carry [c], A. Conrad [d], P. Tamblyn [b], B. Enke [b], J. Christou [d], C. Dumas [e], C.R. Chapman [b], D.D. Durda [b], W.M. Owen [f], W.M. Grundy [g], O. R. Reynolds [a], M.D. Buckman [a]

[a] Air Force Research Laboratory, Kirtland AFB, NM 87117-5771, USA
[b] Southwest Research Institute, 1050 Walnut St. # 300, Boulder, CO 80302, USA
[c] Université Côte d'Azur, Observatoire de la Cote d'Azur, CNRS, Laboratoire Lagrange, France
[d] Large Binocular Telescope Observatory, University of Arizona, Tucson, AZ 85721, USA
[e] TMT Observatory, Pasadena, CA 91124, USA
[f] Jet Propulsion Laboratory, California Institute of Technology, Pasadena, CA 91109, USA
[g] Lowell Observatory, Flagstaff, AZ 86001, USA

ARTICLE INFO

Keywords:
Asteroid Roxane
Asteroid Kalliope
Satellites of asteroids
Adaptive optics
Image processing

ABSTRACT

A definitive orbit is derived for asteroid (317) Roxane's satellite Olympias [S/2009 (317)1] by combining the 2009 discovery images from Gemini North (Merline et al. 2009) with images from Keck and the VLT obtained in 2012, as well as images from its 2016-2017 apparition from the Starfire Optical Range. The orbit is retrograde with respect to the ecliptic but in the same sense as Roxane's spin. Olympias has a period of P=11.9440±0.0005 days, a semi-major axis of a=245±3 km, and an orbital pole at RA=97°, Dec=−71°, or ecliptic coordinates λ=245°, β=−85°, close to the south ecliptic pole. This satellite orbital pole is only 3° from Roxane's orbital pole (but in a retrograde sense) and restricts all observations of Olympias from Earth to within 4° of the satellite's orbital plane. By fitting the brightness ratios between Roxane (rotational period of 8.16961±0.00005 h) and Olympias as a Fourier series, we find a rotational period for Olympias of 8.2587±0.0001 h, making this an asynchronous wide binary. From the brightness ratios, and with the average infrared modeling diameter found in the literature of 19.16±0.39 km (error of the mean), we estimate triaxial ellipsoid radii of 14.5×8.5×7.2 km for Roxane and 3.6×2.5×2.0 km for Olympias. We can then apportion the mass between the two objects and find a density for both (assumed to be the same) of 2.16±0.18 g/cm^3. There are only a few E-type binaries known and this is the first direct determination of E-type density from a binary. We suggest that the system was formed by the Escaping Ejecta Binary (EEB) mechanism of Durda et al. (2004a), probably forming closer together, and then undergoing the complex evolution steps described by Jacobson et al. (2014) involving synchronization, BYORP orbit expansion, loss of tidal lock, and then YORP spinup. Roxane and Olympias may be the only known EEB system to date.

From the same 2016-2017 apparition the orbit of Linus around asteroid (22) Kalliope is derived from the SOR. This well-observed bright satellite is found to have a circular orbit with a period of P=3.5956±0.0004 days, in good agreement with the latest elements of Vachier et al. (2012) of P=3.5957±0.0001 days, and a semi-major axis of a=1099±6 km, somewhat greater than their a=1082±11 km for a slightly eccentric orbit (e=0.007±0.010). With a diameter for Kalliope of 161±6 km (Hanuš et al. 2017), we derive a density for Kalliope of 3.72±0.25 g/cm^3 from our one apparition study, the same as Hanuš et al. (2017) but greater than the 3.24±0.16 of Vachier et al. (2012).

* Corresponding author.
E-mail address: jack.drummond.1.ctr@us.af.mil (J.D. Drummond).

https://doi.org/10.1016/j.icarus.2020.114275
Received 2 August 2020; Received in revised form 15 December 2020; Accepted 17 December 2020
Available online 1 January 2021

1. Introduction

The satellite of (317) Roxane, an E-type asteroid, was discovered by Merline et al. (2009) in 2009 at Gemini North. (See Fig. 1.) Provisionally labeled S/2009 (317)1, it now bears the designation (317) Roxane I, and we have named it Olympias.[1] Further observations were obtained in 2012 at the W. M. Keck Observatory and the European Southern Observatory (ESO) Very Large Telescope (VLT). Over the 2016-2017 northern hemisphere winter season the Starfire Optical Range[2] (SOR) followed Olympias in an attempt to derive an orbit from one apparition (Drummond et al. 2017). However, only by combining these adaptive optics (AO) observations from all four sites have we been able to derive a definitive orbit for Olympias.

Kalliope's satellite Linus, initially called S/2001 (22)1, was discovered in 2001 by Margot and Brown (2001a) at Keck and Merline et al. (2001a) at CFHT. See also Green (2001). Initial system parameters were provided at the 2001 DPS meeting by Merline et al. (2001b) and Margot and Brown (2001b). More system details were then published by Merline et al. (2002) and Margot and Brown (2003). Subsequently, the orbit of Linus became well-determined (Vachier et al. 2012), partly because both Kalliope and Linus are bright, Kalliope at 10th magnitude with a Kalliope/Linus magnitude difference of around 4. Here we present a one-apparition orbit for Linus from SOR-only observations that fits in well with the orbit derived from observations made over years with 8-10 m telescopes (Vachier et al. 2012), just as was done for asteroid (87) Sylvia and its satellite Romulus (Drummond et al. 2016), which demonstrated that the SOR 3.5 m telescope with AO and a sodium laser can be used for satellite imaging.[3]

2. Observatory logs and resolutions

In Appendix B, Tables B.14, B.15, B.16 and B.17 contain the observing logs for the Gemini, Keck, VLT, and SOR observatories, respectively. Measurements for Roxane and Olympias are in Tables B.18, B.19, B.20, and B.21. The observing log and measurement table for Kalliope and Linus at the SOR are in Appendix C.

We made the discovery observations of Olympias in 2009 at the Gemini North telescope with AO in natural guide star (NGS) mode (without a laser), in J-, H-, and K-bands using the NIRI camera (Hodapp et al. 2003) fed by the ALTAIR AO system (Herriot et al. 2000). We next detected Olympias at the 10 m Keck II telescope in 2012 using NIRC2 (van Dam et al. 2004; Wizinowich et al. 2004) in NGS mode at J-, H-, and K- bands. On three nights in 2012, we also detected Olympias at the VLT in the H-band with the NACO system (Lenzen et al. 2003; Rousset et al. 2003), at both a narrow and wide field of view.

At the SOR, as for (87) Sylvia and Romulus (Drummond et al. 2016), for Roxane and Olympias and for Kalliope and Linus, we used two Toptica 20 W sodium lasers to produce 40 W out of the top of the launch telescope in order to create a laser guide star (LGS) for higher order AO correction. Most of the observing was in the J-band at 1.23 μm, but on occasion, when the asteroid was bright, images were obtained in the RI-band at 0.81 μm.

For most of the images we make a simultaneous fit for two Lorentzians since that is the shape of the point spread function (PSF) produced by AO (Drummond 1998, 2014). Furthermore, since neither Roxane nor Olympias were angularly resolved from any telescope, we force the asteroid and satellite PSF to have the same shape, as appropriate for imaging within the isoplanatic patch. In some cases at the SOR, rather than fit simultaneously for two PSFs, we had to fit first the asteroid, and then after subtracting this PSF from the image, we fit a smaller region containing the satellite. The two cases are methods 1 and 3 in Drummond et al. (2016), and are indicated in the measurement table for the SOR in Appendix B. For the Gemini, Keck and VLT images, the fits were always simultaneous.

When Olympias was too close to be clearly seen in an image, the procedure was to use the technique of PSF subtraction, fitting the image for one Lorentzian and subtracting the model. This should leave residuals scattered about zero or reveal Olympias. Alternatively and equivalently, the technique of PSF division was used. Taking the log of the image after dividing by the PSF of Roxane produces residuals also scattered about zero, but sometimes better revealing Olympias. After locating Olympias, both Roxane and Olympias were then fit again for the same shaped PSF to determine position and brightness difference. Similar procedures were used at the SOR for Kalliope and Linus.

We calculate the diffraction limit θ (in radians) of a telescope as a function of observing central wavelength λ_0 and telescope diameter D, as $\theta = \lambda_0/D$, where λ_0 and D are in the same units. We also define a rexel, a resolution element in camera pixels, as the diffraction limit divided by the image scale, rex $= \theta$/scale. The relevant quantity for resolution is the rexel, not the image scale, and in adaptive optics the relevant quantity is the Nyquist sampling, N = rex/(2 pix). For an AO system, N should be unity, that is, there should be two pixels over the fwhm of the PSF, an Airy pattern for the telescope. An oversampled PSF, where rex $>$ 2 pix, or $N>1$, allows for a better determination of the PSF at the expense of poorer signal per pixel, whereas an undersampled PSF, rex$<$2 pix or $N<1$, will not achieve the full telescope resolution. All of the observatories here employ systems that are at or near optimum for AO work, defined by $N\sim1$, or equivalently, rex$\sim$2 pix, as shown in Table 1. There are two magnifications used in front of the NAOS-Conica camera at the VLT that produce two fields of view, narrow (nfov) and wide (wfov), resulting in the two image scales in Table 1. At the SOR the two image scales at two wavelengths are produced by two different cameras over two different optical paths.

3. Roxane and olympias

3.1. Sample images and trefoil

At the SOR we attempted to derive the orbit of Olympias in one apparition, first detecting it on 2016-Oct-12. Irregularly scheduled observations followed over the next 121 days. Positive detections were made at 19 epochs on 8 nights. However, between 2016-Oct-12 and 2017-Feb-10 there were 16 epochs on 9 nights when Olympias was not detected. There were two reasons for this: Roxane faded from its brightest at V = 12.5 to 14.4, compared to V = 10.3–10.9 for Kalliope observed during the same time period, and more importantly, as we show later, the apparent inclination of Olympias' orbit to our line of sight was always around 90° so that it moved in and out of Roxane's PSF. The SOR first detection of Olympias is shown in Fig. 2.

Fig. 3 shows sample images from all four observatories. The image from Gemini is from the night after its discovery, and the image from the VLT is the first, and closest, of Olympias from that observatory. The image from Keck shows a close detection of Olympias, as well as a trefoil-like pattern for the Roxane PSF, similar to the aberrations that plagued most SOR images, although neither the trefoil nor Olympias can

[1] Olympias (375-316 BCE) was the mother of Alexander the Great (Alexander III), king of Macedonia and husband of Roxana, namesake of asteroid Roxane. The satellite is so named because of the role of Olympias in protecting both Roxana and her son (Alexander IV) after the death of Alexander the Great (323 BCE). Roxana and Alexander IV were killed, together, in 309 BCE.

[2] Owned and operated by the Air Force Research Laboratory, Directed Energy Directorate, on Kirtland AFB near Albuquerque, New Mexico.

[3] The SOR authors wish to modify their claim that the SOR 3.5 m telescope is the smallest ground based telescope to image a satellite of an asteroid (Drummond et al. 2016) since Marchis et al. (2003) observed Linus with the Shane 3.0 m telescope in 2001. Although the first asteroid satellite discovered from the ground, Petit-Prince around (45) Eugenia, was made with the slightly larger CHFT 3.6 m telescope by Merline et al. (1999a,b), who also derived initial orbital parameters for the satellite, the SOR still lays claim to have used the smallest ground-based telescope to follow an asteroid's satellite over an apparition and derive its orbit (for Romulus around Sylvia) .

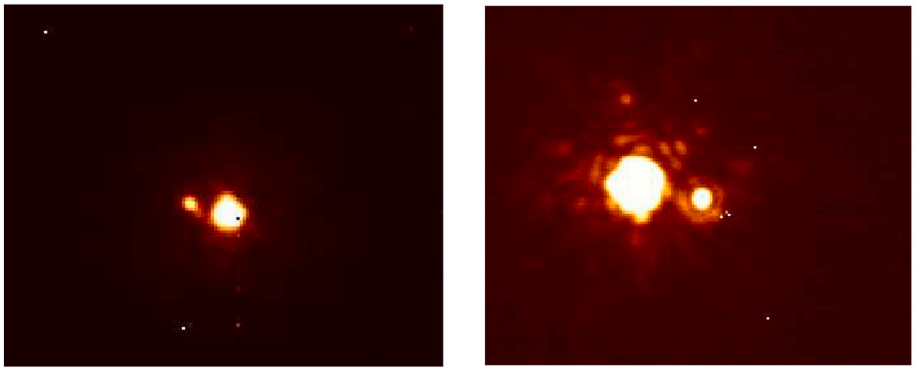

Fig. 1. Unprocessed images of Roxane and Olympias using a linear stretch, focused on mid-level brightness values. Left: 2009-November-24 discovery image of Olympias from Gemini, exactly as seen on our display at discovery. Right: Keck image of the pair on 2012-July-15, using a similar stretch/color scheme, showing the telescope diffraction pattern around Olympias. Separation and magnitude difference for Gemini were $\rho = 0.28''$ and $\Delta K = 3.1$, and for Keck they were $\rho = 0.26''$ and $\Delta K = 2.8$.

Table 1
Observatory resolutions.

Observatory	Band λ_0 (μm)	$\overline{RI}$ (0.81)		J (1.25)		H (1.65)		K (2.1)	
	scale	θ	rex	θ	rex	θ	rex	θ	rex
Tele Diam (m)	($''$/pix)	($''$)	(pix)	($''$)	(pix)	($''$)	(pix)	($''$)	(pix)
Gemini (8)	0.022			0.032	1.5	0.043	2.0	0.054	2.5
Keck (10)	0.009945			0.026	2.6	0.034	3.4	0.043	4.3
VLT (8) wfov	0.02715					0.043	1.6		
VLT (8) nfov	0.01327					0.043	3.2		
SOR (3.5)	0.0165	0.048	2.9						
SOR (3.5)	0.0327			0.027	2.2				

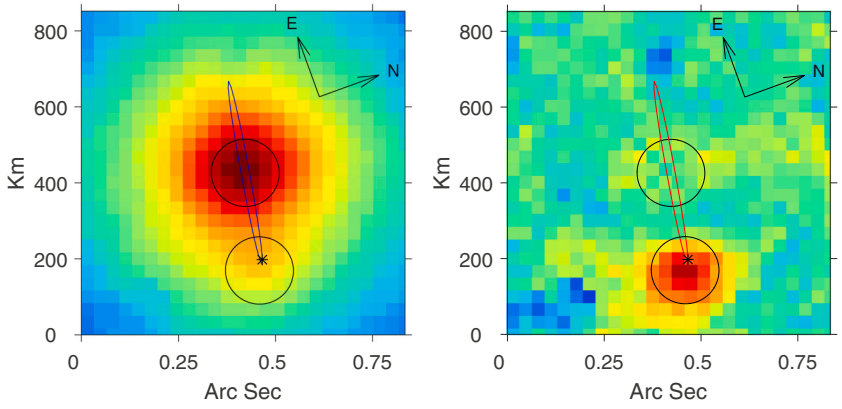

Fig. 2. Images of the first detection of Olympias at the SOR on 2016-Oct-12. At left, on a log brightness scale, Olympias is visible as an extension of Roxane's PSF. At right are the residuals after applying the technique of PSF division (dividing the image by the single PSF Lorentzian model of Roxane and then taking the log) which reveals Olympias. Circles are the Lorentzian PSF diameters at half power for Roxane or Olympias. The plane of the orbit is the elongated ellipse through both figures, illustrating that the orbit was inclined nearly 90° to our line of sight throughout our observing, as we show in Section 3.2.

be seen in the SOR image in Fig. 3. In fact, however, this trefoil, or partial trefoil, can be seen in images from all four observatories (Fig. 4) when the Roxane Lorentzian PSF is divided out. The location of the trefoil-like pattern occurs on the expected location of the first bright diffraction ring in the Keck image in Fig. 1 where the the hexagonal-shaped bright ring diffraction pattern is modified in places by the trefoil. The Gemini image in Fig. 4 also shows one trefoil segment at the expected location of a bright diffraction ring, although the ring itself is not seen. On the VLT and SOR images the trefoil is slightly further from the core of the PSF than where the first ring would be. At Keck, Olympias was well separated from the trefoil, whereas at the SOR and the VLT the satellite was often entangled with it. Not always present, this aberration has been known in AO work, but not well publicized. The cause has been attributed to low wind speeds over the secondary mirror spiders, and recently correction methods have been proposed (Milli et al. 2018; N'Diaye et al. 2018; Sauvage et al. 2016; Vigan et al. 2018; Wilby et al. 2018).

3.2. Orbits for Olympias

Between its discovery at Gemini in 2009 (Merline et al. 2009) and a campaign to observe it through its 2016–2017 apparition at the SOR, we were accumulating observations at Keck and the VLT. Since Olympias was not detected half the time from the SOR it became obvious that we were picking it up only at elongation and it was spending a considerable amount of time lost in the PSF of Roxane. The SOR PSF has inconstant aberrations close to the core, at about the distance of Olympias from Roxane, which often made it difficult to extract the satellite from the aberration. Even at larger telescopes, Gemini and Keck, we made attempts on several other nights to detect the satellite, without success (see notes to Appendix B, Tables B.14 and B.15).

With or without the initial Gemini observations the derived orbit from the SOR was difficult to pin down because it was inclined by about 90 degrees to our line of sight. It could not be determined if the pole was direct or retrograde, or whether the inclination was slightly greater or less than 90 degrees (Drummond et al. 2017). In a broad shallow region of chi-squared space (Figs. 5 and 6), two direct periods emerged, around

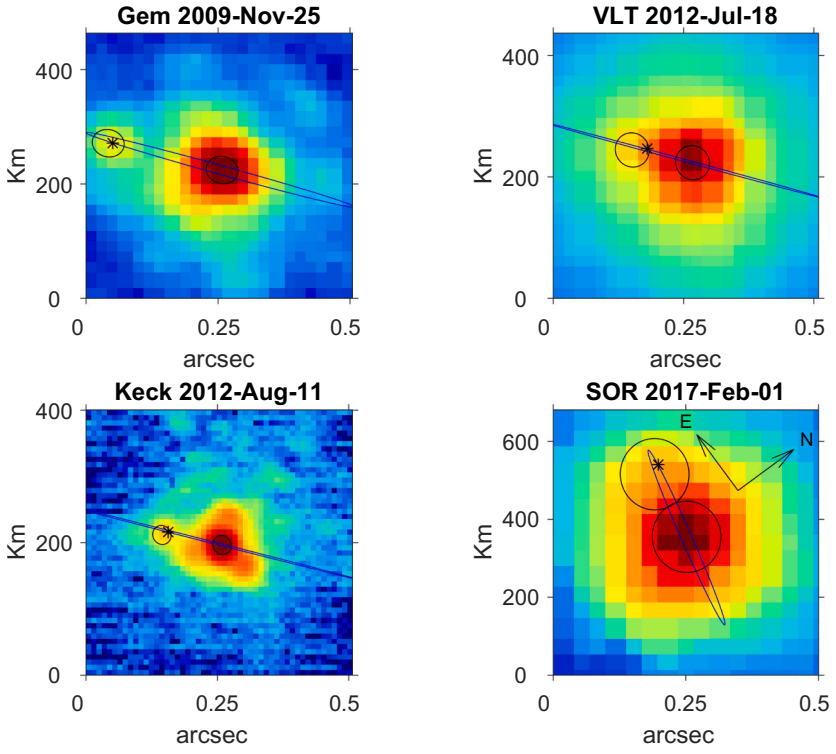

Fig. 3. Images of Roxane and Olympias from all four observatories on a log brightness scale. The orbit is overlaid on each image with the predicted position of Olympias marked by an asterisk, and fwhm PSF circles are drawn around Roxane and Olympias. North is up and east is to the left except for the SOR where it is indicated.

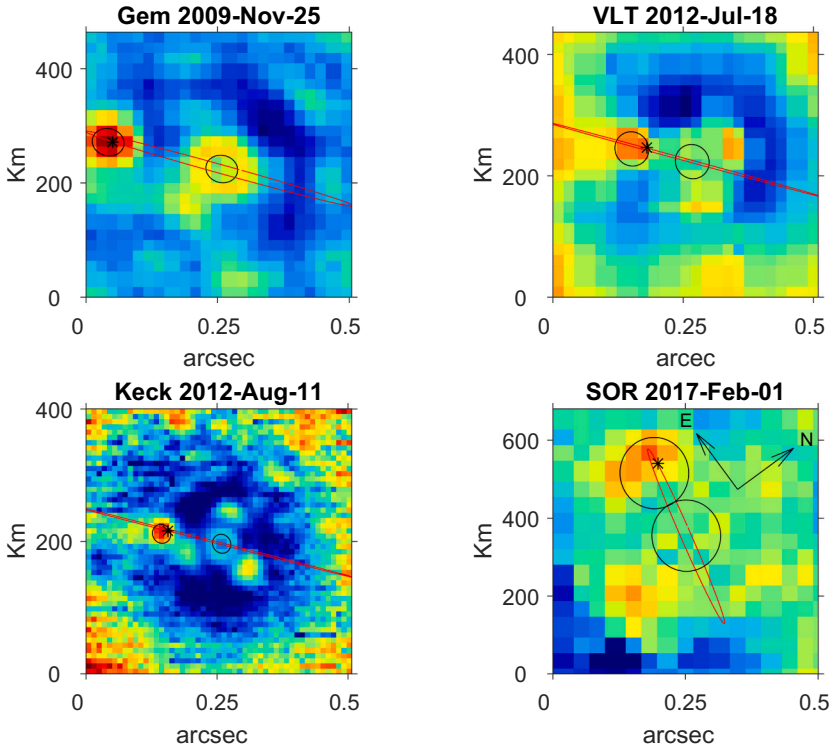

Fig. 4. Same as Fig. 3 except that the Lorentzian PSF of Roxane is divided out, leaving behind Olympias, residuals, and the trefoil. For the SOR and the VLT, Olympias is tangled in the trefoil..

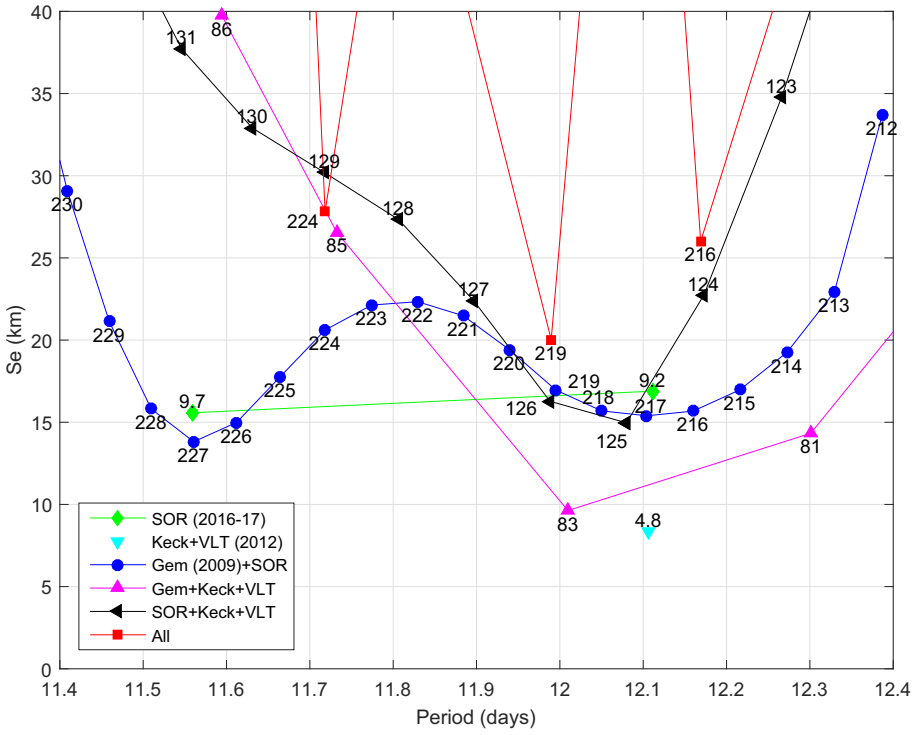

Fig. 5. Direct orbits for Olympias with respect to the ecliptic. Using an initial period found from the number of orbital revolutions between the first and last observations of each combination of SOR, Keck, and Gemini data, we then utilize a non-linear least squares program to iterate to a final orbit for each data set, which includes an adjustment to the initial period. In the figure, the (rounded) number of revolutions is shown next to the point at the final orbital period. Each point represents a local minimum in the chi-squared space, the Standard Error (SE) of fit in km, Eq. (2).

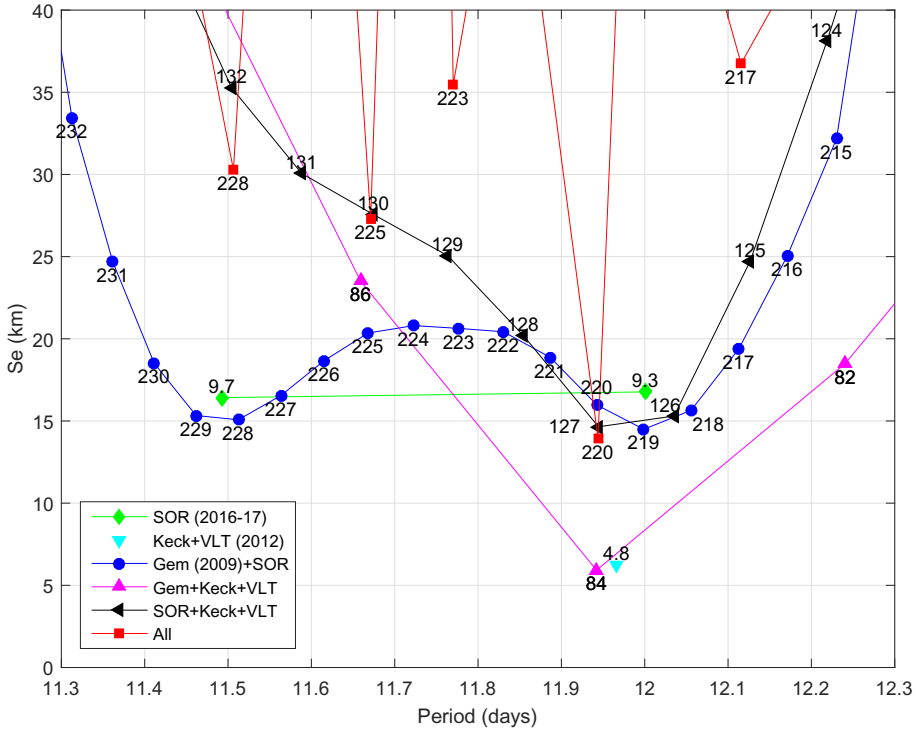

Fig. 6. Retrograde orbits for Olympias with respect to the ecliptic. Same as Fig. 5, but the various combinations of data show more consistent minima at the period of 11.94 days.

11.56 or 12.11 days, and 11.5 and 12.0 days for retrograde periods. For the SOR-only data there were only 9-10 laps of Olympias around its orbit, but for the Gemini plus SOR data there were 217-227 laps for the direct orbit, and 219-228 laps for the retrograde orbit, all leading to the wide shallow spread in chi-squared space. The adopted period is for the global minimum.

However, the Keck and VLT data obtained in 2012 between the Gemini and SOR observations from a much different geometry cleared up the ambiguity or degeneracy even though Olympias was observed over only 4 laps at 16 epochs on 11 nights in the 58 night interval. The ecliptic longitude of Roxane for the Gemini observations was 43°, and ranged from 58-67° for the SOR, but it was the 324-330° range for Keck

Table 2
Olympias elliptical orbital elements EQJ2000 TDB

	SOR	Keck+VLT	Gem+Keck+VLT+SOR
Orbital elements	2016–17	2012	2009; 2012; 2016–17
Number of observations, n	19	16	43
SE (Standard error of fit, km)	16.8	5.8	13.6
a (Semi-major axis, km)	244 ± 7	250 ± 3	245 ± 3
Ω (Right Ascension of ascending node, °)	185.4±1.2	189.0 ± 0.4	186.9 ± 0.7
i (Inclination of orbit to celestial equator, °)	158.3 ± 1.6	161.9 ± 0.5	161.1 ± 0.7
P (Orbital period, days)	12.0007 ± 0.0224	11.9657 ± 0.0148	11.9440 ± 0.0005
T_q (Time at periapsis passage, JD)	2457688.16 ± 0.25	2457679.96 ± 1.75	2457688.47 ± 0.23
e (Eccentricity)	0.146 ± 0.052	0.067 ± 0.022	0.074 ± 0.012
ω (Argument of periapsis, °)	311.7 ± 5.5	339.4 ± 22.4	315.3 ± 6.5
$\mathscr{M}$ (Total Mass, $\times 10^{18}$ kg)	8.00 ± 0.69	8.65 ± 0.31	8.17 ± 0.30
Pole J2000			
RA (Right Ascension, °)	95.4	99.0	96.9
Dec (Declination, °)	−68.3	−71.9	−71.1
σ (Pole uncertainty, °)	1.5	0.5	0.8
λ (ecliptic longitude, °)	222.1	243.0	244.5
β (ecliptic latitude, °)	−87.3	−83.8	−84.8
M at 2000.0 (Mean anomaly, °)	36	103	232
M at 2017.0 (Mean anomaly, °)	183	75	183

and VLT that led to a definitive retrograde orbit with a period of 11.94 days. Table 2 shows the progression of orbit determinations, from single apparition orbits to the adopted orbit using images from Gemini, Keck, VLT and SOR.

Part of the reason for the better orbit with Keck data is that Olympias was imaged outside of the Roxane PSF aberrations, unlike in the images from the SOR (and VLT). For example, the average separation between Kalliope and Linus during this time was 0.60″, and for Sylvia and Romulus 0.55″ (Drummond et al. 2016), both yielding one-apparition orbits from the SOR comparable to previously determined orbits. However, for Roxane and Olympias the average separation was only 0.19″ (Table B.21), within the trefoil-like aberration at the SOR, but outside it from Keck (Table B.19) where the average was 0.23″.

Table 2 lists the orbital elements found from an analytic non-linear least squares fit of x and y in km as a function of time, converted from position angles (*PA*) and separations (*Sep*) in km

$$x = cos(PA)cos(Dec)\ \ Sep \quad ; \quad y = sin(PA)cos(Dec)\ \ Sep \tag{1}$$

for single apparition observations and for all data. *SE* is the Standard Error of Fit

$$SE = \sqrt{\frac{\sum (x - x')^2 + \sum (y - y')^2}{2n - 7}} \tag{2}$$

where x' and y' are the predicted values from the fit, n is the number of observations where each observation produces one x and one y, and 7 is the number of orbital elements, a, Ω, i, P, T_q, e, and ω, in Table 2. Uncertainties on the elements come from the covariance matrix produced by the least squares program (Bevington and Robinson 2003). The mean anomaly M is given for two times, for the middle of the SOR observations and for a more standard epoch of 2000-Jan-1 12h TDB (Archinal et al. 2018).

Table 3 gives the acute angle between Olympias' adopted orbital pole and Roxane's orbital pole and each of the two solutions for Roxane's spin poles from the DAMIT[4] web site. However, fitting the models associated with these spin poles as ellipsoids shows that the spin axes are not aligned with the axes of maximum moments of inertia, differing by 14° and 9°, respectively. If indeed the equator of Roxane and the orbital plane of Olympias are inclined by the ∼24° in Table 3, then, as far as we now know, this is the only case where an asteroid's satellite is not in the equatorial plane of the primary. Since the ecliptic latitude of Roxane's orbital pole (+88.2°) is within 2° of the ecliptic north pole, all observations of Roxane from Earth will be constrained to lie within 2° of its orbital plane, and given the location of the satellite's orbital pole and the asteroid's orbital pole, all observations of Olympias from Earth will also be near its orbital plane around Roxane, within 3.4° of the Olympias' orbital plane.

[4] https://astro.troja.mff.cuni.cz/projects/damit/, Ďurech et al., 2010.

Table 3
Obliquities with Table 2 Gem+Keck+VLT+SOR ecliptic Pole (ECJ2000).

Pole	$\lambda°$	$\beta°$	Obliquity° (acute)
Roxane orbital	61.4	+88.2	3.4
Roxane rotational (solution 1)	40	−70	24.8
Roxane rotational (solution 2)	220	−62	23.4

3.3. Mass, volume and density

3.3.1. Roxane as a single body

With the mean diameter from infrared studies of Roxane (Table 4) of $\mathscr{D} = 19.16 \pm 0.39$ km (where the uncertainty is the error of the mean), and assuming all of the mass from Kepler's laws for binary orbits resides in Roxane, Table 5 lists its volume, calculated as $\mathscr{D}^3\pi/6$, and mass and bulk density for the two single apparition solutions and for the total data orbit solutions from Table 2.

3.3.2. Two spheres

On the other hand, in light of the relatively small magnitude differ-

Table 4
The diameter estimates ($\mathscr{D}$) of (317) Roxane collected in the literature. For each, the 1 σ uncertainty, method, and bibliographic reference are reported. The methods are NEATM: Near-Earth Asteroid Thermal Model and STM: Standard Thermal Model. The weighted average and weighted standard deviation are reported, where the weight is $1/\sigma^2$ for each determination. For propagating the uncertainties with the diameter, the error of the mean is used, $\sigma/\sqrt{n} = 0.39$ km.

$\mathscr{D}$	σ	Method	Reference
18.67	1.40	STM	Tedesco et al. (2004)
19.86	0.12	NEATM	Masiero et al. (2011)
15.25	0.56	NEATM	Masiero et al. (2012)
20.41	1.99	NEATM	Pravec et al. (2012)
16.88	0.39	NEATM	Usui et al. (2013)
18.65	0.16	NEATM	Masiero et al. (2014)
16.54	1.65	NEATM	Alí-Lagoa et al. (2018)
18.87	3.77	NEATM	Alí-Lagoa et al. (2018)
19.16	1.12	Average	

Table 5
Roxane mass, volume and bulk density.

	SOR	Keck+VLT	Gem+Keck+VLT+SOR
Mass (g)	$8.00 \pm 0.69 \times 10^{18}$	$8.65 \pm 0.31 \times 10^{18}$	$8.17 \pm 0.30 \times 10^{18}$
Volume (cm^3)	$3.68 \pm 0.22 \times 10^{18}$	$3.68 \pm 0.22 \times 10^{18}$	$3.68 \pm 0.22 \times 10^{18}$
Density (g/cm^3)	2.17 ± 0.23	2.35 ± 0.17	2.22 ± 0.16

ence between Roxane and Olympias, rather than assume that all of the mass resides in Roxane, we should distribute the total mass derived from the orbit between Roxane and Olympias. Furthermore, since all observations are confined to being in or near Roxane's equatorial plane (Section 3.2), the diameter in Table 4 must be from the sum of the average areas of Roxane and Olympias in Roxane's equatorial plane, or in terms of the effective radius ($r_e = \mathscr{D}/2 = 9.58$ km)

$$r_e^2 = r_R^2 + r_O^2 = 9.58^2 \tag{3}$$

where the subscripts denote Roxane or Olympias. Converting the magnitude differences between Roxane and Olympias from Tables B.18-B.21 into ratios of areas and fitting these as a brightness difference lightcurve (see Appendix A) yields an average brightness ratio q (the square root of the first term in Eq. (A4) in Appendix A) in the equatorial plane of

$$q = r_R^2/r_O^2 = 13.71 \tag{4}$$

for a mean magnitude difference of 2.8 between Roxane and Olympias. Solving Eqs 3 and 4 for r_R^2 and r_O^2 yields

$$r_R^2 = r_e^2 \; q/(q+1) \quad ; \quad r_O^2 = r_e^2 \; /(q+1) \quad . \tag{5}$$

We can estimate individual volumes by raising the individual mean equatorial areas to the 1.5 power (this assumes both are spheres), and summing to obtain the total volume in the system

$$V = \left[r_e^3 q^{1.5} \Big/ (1+q)^{1.5} + r_e^3 \Big/ (1+q)^{1.5} \right] \; 4\pi/3 \quad . \tag{6}$$

Assuming the same albedo for Roxane and Olympias at all wavelengths (DeMeo et al. 2011; Yang et al. 2016; Polishook et al. 2009), as well as the same density for both, the total mass $\mathscr{M}$ from the orbit will be distributed as the volume

$$\mathscr{M} = \mathscr{M} \; q^{1.5} \Big/ (1+q)^{1.5} + \mathscr{M} \Big/ (1+q)^{1.5} \quad . \tag{7}$$

The semi-major axes of the true orbit about the center of gravity are distributed similarly, but in reverse

$$\alpha = \alpha_R + \alpha_O = \alpha \; \Big/ (1+q)^{1.5} + \alpha \; q^{1.5} \Big/ (1+q)^{1.5} \quad . \tag{8}$$

Table 6 then shows, only for all data, the breakdown of Table 5 into individual components. The density is 7% greater than in Table 5.

3.3.3. Two Triaxial Ellipsoids

Rather than extrapolate the equatorial areas to volumes by raising the areas to a power, it is more accurate to use a triaxial ellipsoid model with radii $a \geq b \geq c$, as developed in Appendix A. The key is to constrain the b/c ratios to values between the prolate spheroid case ($b/c = 1$) and the hydrostatic equilibrium case. This, then, results in Table 7, which

Table 6
Individual spherical Roxane and Olympias masses, semi-major axes, volumes and bulk densities.

Gem + Keck + VLT + SOR	Roxane	Olympias
Mass ($\times 10^{18}$ g)	8.02±0.30	0.16±0.01
True semi-major axis (km)	4.7±0.2	240±3
Volume ($\times 10^{18}$ cm^3)	3.31±0.22	0.07±0.01
Density (g/cm^3)	2.42±0.18	2.42±0.18

Table 7
Triaxial ellipsoid results.

Parameter	Roxane	Olympias
Mass ($\times 10^{18}$ g)	8.01±0.30	0.16±0.01
True semi-major axis (km)	4.9±0.4	240±3
a radius (km)	14.5±1.1	3.6±0.3
b radius (km)	8.5±0.7	2.5±0.2
c radius (km)	7.2±0.6	2.0±0.2
Volume ($\times 10^{18}$ cm^3)	3.71±0.28	0.08±0.01
Density (g/cm^3)	2.16±0.18	2.16±0.18

provides the first estimate for the density of an E-type asteroid from a satellite orbit. The uncertainties in the table are not formal σ's, but are the range of the values from Table A.13. We also note that the Roxane/Olympias barycenter circles inside of Roxane, a third of the way to the surface along the a axis, and a little over halfway along the b axis.

Triaxial ellipsoid fits of the Roxane DAMIT models lead to an axial ratio of $a/b = 1.65$, and $b/c = 1.07$ or 1.16, although, as pointed out in Appendix A, the b/c ratio cannot be found from equatorial-only observations. Nevertheless, these two models are in good agreement with Table 7. Their a/b ratio of 1.65 produces an equatorial lightcurve amplitude of 0.54 magnitudes for Roxane compared with our a/b=1.71 for an equatorial amplitude of 0.58 magnitude, a discrepancy arising from the difference in rotational poles for Roxane, the former determined from lightcurves, the latter from the satellite's orbit.

3.4. Discussion of formation

Immediately upon acquiring the discovery image of this binary system, we realized that this was a wide binary, having gross characteristics of several other wide systems that we had discovered. It had a widely separated secondary (estimated then at ≥25 primary radius, R_p), and a relatively small size ratio (estimated then at R_O/R_p=0.26). Both of these characteristics were reported in our discovery IAUC (Merline et al. 2009), in addition to speculations about how this system and the other wide binaries (listed therein) were showing characteristics expected of systems created by the Escaping Ejecta Binary (EEB) mechanism studied and promoted by Durda et al. (2004a,b).

In contrast, it was distinctly different from other binaries that had been discovered around large (≥30 km) primaries, which have relatively small satellites in tight (~10 Rp) orbits. Those systems we attributed to the SMAshed Target Satellite (SMATS) mechanism where the small satellite remains bound to the original target, also studied by Durda et al. in the same paper. Both the SMATS and EEB formation result from energetic collisions. The EEBs are formed when two fragments leave the scene of the catastrophic collision with closely similar velocity vectors so that they are bound by their mutual gravity. Durda et al. (2004a) showed that many hundreds of EEBs could be stable outcomes of a single collision and thus were expected to be common.

Soon afterward, Durda et al. (2010) provided more support for the idea that these wide systems were produced by the EEB mechanism, by comparing their model runs directly with actual individual binary systems, and showing that they were distinct from the SMATS. In some regimes of the parameter space, however, the characteristics overlapped (tight systems with similar-sized components), and either mechanism would have been allowed, based on those few characteristics alone.

Over the decade before our discovery of the Roxane system, much development had been done on how the YORP mechanism (Scheeres 2007) and the related Binary YORP (BYORP) mechanism (Ćuk and Burns 2005) could account for the formation of small binaries in both the NEA region and the Main Belt, and dramatically affect the evolution of those systems. Polishook et al. (2011) set out to determine whether in fact the wide binaries from Durda et al. (2010) could have instead been produced by YORP spin-up of a rubble pile asteroid to the limit at which it would fission into a binary system, and then subsequently evolve. He showed, convincingly, that most of the wide binaries listed in our

discovery IAUC, plus some others, could be formed by YORP rather than as EEBs. The most compelling piece of evidence was that most of the primaries were spinning very rapidly, indicating that they probably had been spun up to fissionable speed. Curiously, Roxane was one of the systems that did not have a fast rotation. It has a spin period of 8.2 h (Hanuš et al. 2016), while the others are spinning only modestly slower than the rotational-fission limit of 2.2 h (Walsh et al. 2008; Pravec et al. 2010).

Another issue with Roxane is its size. With a diameter of about 19 km, it is expected to be near the limit of where YORP could significantly affect the spin. Certainly, the time scale would be far longer than for most of the others studied, which are a few kilometers in size. However, Hanuš et al. (2013a) showed that main-belt objects of size $\leq$30 km were affected enough by YORP to drive their obliquities significantly, clustering near both ecliptic poles, but with a stronger effect toward the southern pole. Roxane, in fact, does have a retrograde spin (relative to the ecliptic), with latitude at -62° or -70°, while the Olympias orbit pole is near -85°.

Polishook et al. (2011) further point out that the time scales for spin-up and evolution by YORP/BYORP of the systems around primaries of size $\leq$10 km are so short that they would have destroyed any pre-formed EEBs, which would have formed on timescales more consistent with the much longer collisional regime. This might explain the relative paucity of observed EEB systems. The YORP production of a secondary from the much larger Roxane primary would be less likely and thus spare that system, if formed as an EEB, from destruction.

While there may be a diminished effect of YORP on Roxane itself, there should still be effects of YORP/BYORP on the secondary (diameter 5 km) and its orbit, possibly lasting over the long time since the binary was created as an EEB. This may be evidenced by the slow spin of Roxane, and moderate southern pole position, while the orbit of Olympias is nearly at the southern pole.

In a separate study, Polishook (2012) estimated the likely pole orientation of primaries of many small binary systems. Although Roxane was not included in that study, he found that there appeared to be a preference for retrograde spins. Systems formed by collisions should show no preference. We know that Roxane's spin is at a high southern latitude. In that sense, the spin pole of Roxane really gives us little help on the formation mechanism. Its pole could have resulted from either mechanism.

Jacobson et al. (2014), in a proposed series of processes involving YORP spinup and BYORP evolution, also come to the conclusion that the Roxane system was not likely to be created by YORP spin-up. Instead, they suggest that it may be the one example likely to be formed by the EEB mechanism. The complex steps that go into the evolution of a binary, once formed, would influence the present characteristics of any system, and particularly more so in a system in which the primary is less affected by YORP than the secondary.

Jacobson et al. (2014) claim that production by either EEB or YORP should have resulted in a relatively high eccentricity. From their equations, they would expect e$\sim$0.9 if formed by YORP and that it would be unlikely to be damped by tidal effects. We estimate from Durda et al. (2004a) that the chances of an EEB produced initially with the eccentricity of Olympias' orbit of 0.07 would be around 2%. We point out, however, that a higher eccentricity could have been damped more by tidal effects had it formed with a smaller semi-major axis than it now has or that the eccentricity could have been damped subsequently by YORP/BYORP. Ćuk and Burns (2005) claim that small, but non-zero, eccentricities (like this system) can result from YORP/BYORP. Most of the larger binary systems have nearly zero eccentricity, presumably in those cases, from tides.

Our measurements of the spin period of the secondary, at 8.3 h (Appendix A.2 and Fig. A.9), indicate that it is currently not synchronous with the orbit, making this an asynchronous wide binary. As such, we suggest that it formed as an EEB, closer to Roxane, and possibly with higher eccentricity. Tidal effects could have rapidly brought the satellite into synchronization and damped the eccentricity. In the mechanism described by Jacobson et al. (2014), BYORP could have then allowed the orbit to evolve to a wide orbit. Eventually, synchronization could be lost, BYORP would then turn off, and YORP could act to spin up the satellite to its current rate.

Walsh and Jacobson (2015), in a review paper, also list the Roxane system as perhaps the only known EEB system. We concur with the analyses above, with the possible addition that YORP/BYORP could have further modified the characteristics of the Roxane system, likely formed long ago, so that it may not now show entirely the characteristics of what one might expect of an EEB system formed initially with random orbit orientation and higher orbital eccentricity. YORP on both components would be affected by the size of the components, the solar distance, and the higher albedo and thermal characteristics of an E-type object. We show here that both the primary and secondary are non-spherical and the characteristics strongly hint that it was formed as an EEB, but subsequently modified over a long time scale by YORP/BYORP, but not nearly as efficiently as smaller systems. YORP/BYORP would have no influence over the larger main-belt binaries. Thus, Roxane may reside in a sweet spot where it still retains the fingerprints of being formed as an EEB, but not unmodified by the primary mechanism that forms and completely modifies smaller systems. It may provide a rare system by which to understand EEB formation and the limits of YORP/BYORP.

4. Kalliope and Linus

From 2016-Nov-7 through 2017-Feb-10 at the SOR, an interval of 95 nights, we obtained 44 sets of observations of Kalliope at 17 epochs on 11 nights. Each set consists of an average of between 2 and 42 images at the same exposure, either 0.6, 1.9, 5, 10, or 20 s. Each set was measured, and the measurements averaged for sets close together in time to comprise an epoch, 1-4 epochs per night. Altogether, 582 images were obtained for a total exposure of 3383 s on Kalliope and Linus. Examples are shown in Fig. 7, our first and last detections of Linus, and Fig. 8, the image at the smallest separation between Kalliope and Linus.

4.1. Orbits for Linus

Initially guided by only the orbital period of Vachier et al. (2012), we derive an EQJ2000 celestial equatorial orbit for Linus about Kalliope by minimizing the x and y residuals in km, converted from the position angles (*PA*) and separations in km (*Sep*) in Table C.23, $x = \cos(PA)\cos(Dec)\,Sep$ and $y = \sin(PA)\cos(Dec)\,Sep$. Thus, each observation or image produces two independent quantities for a non-linear least squares program that also produces uncertainties on the orbital elements. Just as for Romulus around Sylvia (Drummond et al. 2016), an eccentricity could not be found since the program would not converge if it were included. Therefore, our initial epoch Julian Day of T_{Ω} in the table of orbital elements, Table 8, refers to the time of passage of Linus through the celestial equator near the middle of our observations.

For comparison, the latest orbit determination from Vachier et al. (2012) is also included in the table. From 52 observations over a decade, mostly from 8-10 m telescopes with AO, they used essentially a Monte Carlos approach with a genetic algorithm to find the elements, and reported uncertainties at a 3σ level, which we reduce to one σ to compare with our results. Although they found a low eccentricity of 0.007 ± 0.010, the fact that this uncertainty is greater than the eccentricity itself reinforces our interpretation that the orbit is circular. The agreement between their angular elements and ours is very good, but they found a slightly smaller orbit and longer orbital period. Because their baseline was some 10 years compared to our 95 days, their orbital period is much better determined. We find no evidence for nodal precession as suggested by Marchis et al. (2003).

In Table 8, the initial epoch refers to the Julian Date (JD) of periapse passage (T_q) for an elliptical orbit or to the time of nodal passage (T_{Ω}).

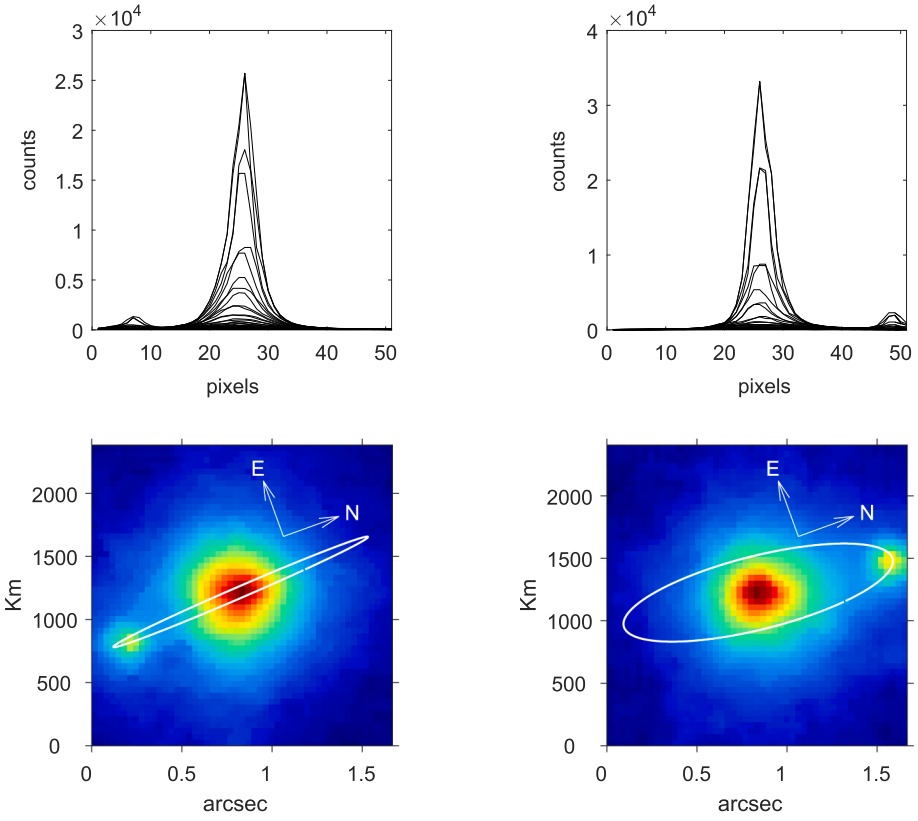

Fig. 7. Images and profiles from the first (left) and last (right) nights of observations of Linus. The profiles are plotted on a linear scale, in camera counts vs. pixels, while the images are shown on a log scale. North and east are shown on the images, as well as the apparent ellipse of the orbit.

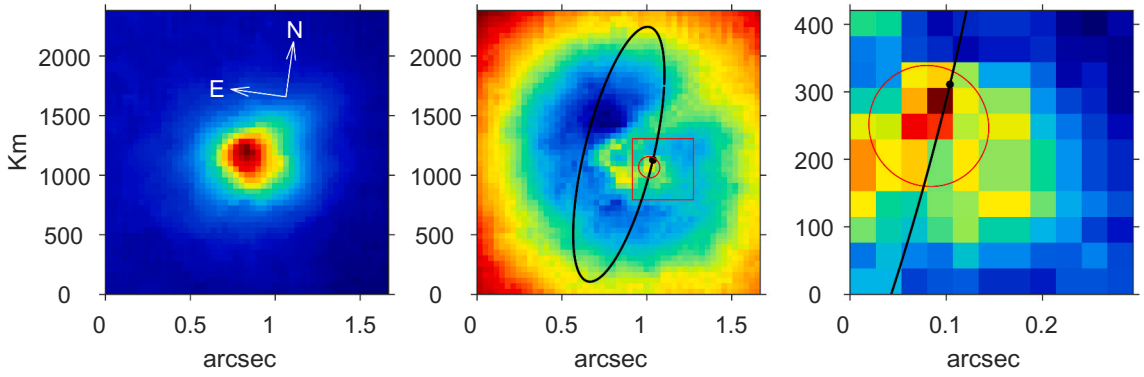

Fig. 8. Images at the smallest separation between Linus and Kalliope on 2017 Feb 9. All images are on a log scale. At left is the original image, in the middle is the log of the image divided by the model PSF of Kalliope, and at right is a closeup from the middle. The orbit is drawn on the middle and right images, as well as the fwhm PSF circle at the measured position of Linus ; its predicted position is a dot on the orbit.

Following the recommendations of Archinal et al. (2018) for an initial epoch of JD = 2451545 = 2000.0 = 2000 Jan 1 12h TDB, we calculate mean anomalies, m_Ω, for this time from T_Ω and the period: m_Ω = 360° (2451545 − T_Ω)/P, modulo 360°. The difference in orbital periods leads to the difference in mean anomalies of Linus in the last entries of Table 8, where the 16° difference between these m_Ω's reflects the short extrapolation from the Vachier et al. time zero-point in 2001 Nov to 2000 Jan compared to our longer extrapolation from 2017 to 2000 with a different period. Going the other way, extrapolating to a time during our observations, the difference in m_Ω's on 2017 Jan 1 12h TDB, measured from the nodal passage, is only 2°. (Add 0.1° to the m's to convert from Barycentric Dynamical Time (TDB) to UTC).

4.2. *Kalliope's density*

Extending the compilations of Carry (2012), Tables 9 and 10 give the diameters and masses for Kalliope collected from the literature, and their averages. We choose to adopt the diameter from Hanuš et al. (2017), since it encompass the most techniques. Assuming all of the mass (from Kepler's laws for binary orbits) resides in Kalliope, Table 11 lists Kalliope's bulk density using the mass from our study of the satellite's orbit and with the diameter of Kalliope from Hanuš et al. (2017). The mass, volume, and density of Kalliope from other recent determinations are also given in the table, where the errors on the quantities from Vachier et al. (2012) are their errors divided by 3 since they give them as 3σ. The two earlier studies arrived at lower densities

Table 8
Linus orbital elements EQJ2000 TDB.

	This paper	Vachier et al. (2012)
Number of observations, n	17	52
SE (Standard error of fit, ″)	0.014	0.015
a (Semi-major axis, km)	1098.6±6.1	1081.5±11.2
Ω (Right Ascension of ascending node, °)	284.30±0.34	285.05±0.70
i (Inclination of orbit to celestial equator, °)	94.18±0.42	94.18±0.64
P (Orbital period, days)	3.595606±0.000375	3.595712±0.000068
T_q (Time at periapse passage, JD)	–	2452215.141±0.022
T_Ω (Time at nodal passage, JD)	2457751.021±0.004	2452217.239±0.022
e (Eccentricity)	0	0.006883±0.010413
ω (Argument of periapse, °)	0	150.32±2.4
$\mathscr{M}$ (Total Mass, $\times 10^{18}$ kg)	8.13±0.14	7.75±0.23
Pole J2000		
RA (Right Ascension, °)	194.30	195.05
Dec (Declination, °)	−4.18	−4.18
σ (Radius of pole uncertainty, °)	0.4	0.7
λ (ecliptic longitude, °)	194.79	195.47
β (ecliptic latitude, °)	1.78	2.07
M_Ω at 2000.0 (Mean anomaly from node, °)	359.4	15.9
M_Ω at 2017.0 (Mean anomaly from node, °)	323.2	321.4

Table 9
The diameter estimates ($\mathscr{D}$) of (22) Kalliope collected in the literature. For each, the 1 σ uncertainty, method, and bibliographic reference are reported. The methods are adam: Multidata 3-D Modeling, lcimg: 3-D Model scaled with Imaging, lcocc: 3-D Model scaled with Occultation, occ: Occultation, neatm: Near-Earth Asteroid Thermal Model, stm: Standard Thermal Model, tpm: Thermophysical Model. The weighted average and weighted standard deviation are reported, where the weight is $1/\sigma^2$ for each determination.

#	$\mathscr{D}$ (km)	σ (km)	Method	Reference
1	174.000	17.400	STM	Morrison and Zellner (2007)
2	167.000	17.000	NEATM	Magri et al. (2007)
3	181.000	4.600	STM	Tedesco et al. (2004)
4	162.672	5.001	STM	Ryan and Woodward (2010)
5	183.114	7.848	NEATM	Ryan and Woodward (2010)
6	167.000	15.296	NEATM	Masiero et al. (2011)
7	143.000	10.000	LCOCC	Ďurech et al. (2011)
8	190.570	4.630	NEATM	Masiero et al. (2012)
9	170.300	23.400	NEATM	Marchis et al. (2012)
10	167.000	17.000	TPM	Marchis et al. (2012)
11	139.780	2.140	STM	Usui et al. (2013)
12	148.000	17.000	LCIMG	Hanuš et al. (2013b)
13	167.540	3.050	NEATM	Masiero et al. (2014)
14	161.000	6.000	ADAM	Hanuš et al. (2017)
15	143.290	14.330	NEATM	Alí-Lagoa et al. (2018)
16	133.520	26.700	NEATM	Alí-Lagoa et al. (2018)
17	144.861	20.657	OCC	Herald et al. (2019)
18	152.832	13.287	OCC	Herald et al. (2019)
19	142.614	2.300	OCC	Herald et al. (2019)
20	133.538	6.131	OCC	Herald et al. (2019)
	153.54	17.44	Average	
	161.00	6.00	Adopted	Hanuš et al. (2017)

because they utilized lower masses and higher volumes, but the table also shows that even with our short arc, smaller telescope data can be comparable to data from larger telescopes over longer intervals.

5. Summary

After demonstrating with Sylvia and Romulus (Drummond et al. 2016) that smaller telescopes (~4 m) can follow an asteroid's satellite over one apparition to derive an orbit comparable to decades of observations with large (8–10 m) telescopes, we show this again here with Kalliope and Linus observed with the SOR's 3.5 m telescope over the 2016–2017 apparition. For Kalliope we find a density of 3.72±0.25 g/cm^3 for a Kalliope diameter of 161±6 from Hanuš et al. (2017). The standard error of fit for the SOR orbit of Linus is 14 mas, comparable to the 15 mas standard error of Vachier et al. (2012) derived with the larger telescopes, and justifies including the SOR measurements of Olympias around Roxane with 8-10 m telescopes.

In another attempt to derive an orbit in one observing season, over the same 2016–2017 apparition, the SOR observed Roxane and its satellite Olympias, discovered in 2009 at Gemini (Merline et al. 2009). Because Olympias remained so close to Roxane, in an orbit inclined 90° to our line of sight, it was difficult to find an orbit from only the SOR. However, by adding the Gemini observations from the discovery apparition in 2009, and from Keck and VLT in 2012, the first definitive orbit has been found, with a period of 11.9440±0.0005 days and a pole very close to the ecliptic south pole. Because both Roxane and Olympias orbit nearly in the ecliptic, Olympias' orbit will always be seen inclined nearly 90° to our line of sight. Assuming that all of the mass determined from the orbit is in Roxane, and using an average infrared modeling diameter from the literature for Roxane of 19.16±0.39 (error of the mean) km, we would derive a density of 2.22±0.16 g/cm^3.

Although the orbit of the satellite would be inclined some 24° to Roxane's equator for the Roxane spin poles on the DAMIT web site, if we assume that Roxane and Olympias are triaxial ellipsoids and not spheres, have the same albedo and density, and have always been observed near or in in their equatorial planes, then the brightness difference between the two leads to a rotational period for the satellite of 8.2587 h (making this system a wide asynchronous binary), yielding a lower density for both of 2.16 ± 0.18 g/cm^3, with radii of 14.5 × 8.5 × 7.2 km (19 km spherical-equivalent diameter) for Roxane, and 3.6 × 2.5 × 2.0 km (5 km diameter) for Olympias. This density is the first estimate for an E-type asteroid from a satellite orbit. We suggest that the system was formed by the Escaping Ejecta Binary (EEB) mechanism of Durda et al. (2004a), subsequently modified by BYORP/YORP, and may be the only known EEB system. Roxane and Olympias may also be the only known case where a satellite is inclined to the asteroid's equator.

Table 10
The mass estimates ($\mathscr{M}$) of (22) Kalliope collected in the literature. For each, the 1 σ uncertainty, method, and bibliographic reference are reported. The methods are bgeno: Binary: Genoid, bimg: Binary: Imaging, defl: Deflection, ephem: Ephemeris. The weighted average and weighted standard deviation are reported, where the weight is $1/\sigma^2$ for each determination.

#	$\mathscr{M}$ass (kg)	Method	Reference
1	$(7.30 \pm \ \ - \ -) \times 10^{18}$	BIMG	Merline et al. (2002)
2	$(7.36 \pm 0.44) \times 10^{18}$	BIMG	Margot and Brown (2003)
3	$(1.69 \pm 0.56) \times 10^{19}$	DEFL	Kochetova (2004)
4	$(8.15 \pm 0.26) \times 10^{18}$	BIMG	Descamps et al. (2008)
5	$(8.09 \pm 0.20) \times 10^{18}$	BIMG	Marchis et al. (2008)
6	$(7.36 \pm 0.74) \times 10^{18}$	EPHEM	Folkner et al. (2009)
7	$(13.30 \pm 5.18) \times 10^{18}$	DEFL	Zielenbach (2011)
8	$(13.10 \pm 3.76) \times 10^{18}$	DEFL	Zielenbach (2011)
9	$(13.10 \pm 3.84) \times 10^{18}$	DEFL	Zielenbach (2011)
10	$(2.09 \pm 0.71) \times 10^{19}$	DEFL	Zielenbach (2011)
11	$(7.75 \pm 0.23) \times 10^{18}$	BGENO	Vachier et al. (2012)
12	$(1.67 \pm 0.13) \times 10^{19}$	EPHEM	Fienga et al. (2013)
13	$(4.77 \pm 0.79) \times 10^{18}$	DEFL	Goffin (2014)
14	$(7.50 \pm 70.90 \times 10^{16}$	EPHEM	Viswanathan et al. (2017)
15	$(6.40 \pm 2.01) \times 10^{18}$	EPHEM	Fienga et al. (2020)
	$(7.73 \pm 1.74) \times 10^{18}$	Average	
	$(8.13 \pm 0.14) \times 10^{18}$	Adopted	This paper, Table 8

Table 11
Kalliope mass, volume and bulk density.

	This paper, mass from orbit Vol from Hanuš et al. (2017)	Hanuš et al. (2017)	Vachier et al. (2012)	Carry (2012)
Mass ($\times 10^{21}$ g)	8.13 ± 0.14	8.1 ± 0.2	7.75 ± 0.23	7.96 ± 0.31
Volume ($\times 10^{21}$cm^3)	2.19 ± 0.14	2.19 ± 0.14	2.40 ± 0.09	2.58 ± 0.27
Density (g/cm^3)	3.72 ± 0.25	3.7 ± 0.4	3.24 ± 0.16	3.08 ± 0.58

Declaration of Competing Interest

None.

Acknowledgments

While all observations reported in this paper were acquired by the co-authors, we wish to thank the New Horizons team for supporting our shared Keck time in the summer of 2012, and to acknowledge the assistance of TeamKeck in providing some of our observing time through the Keck Director.

The W. M. Keck Observatory is operated as a scientific partnership among the California Institute of Technology, the University of California and the National Aeronautics and Space Administration. The Observatory was made possible by the generous financial support of the W. M. Keck Foundation. The authors wish to recognize and acknowledge the very significant cultural role and reverence that the summit of Mauna Kea has always had within the indigenous Hawaiian community. We are most fortunate to have the opportunity to conduct observations from this mountain.

The Gemini Observatory is operated by the Association of Universities for Research in Astronomy, Inc., under a cooperative agreement with the NSF on behalf of the Gemini partnership: the National Science Foundation (United States), the National Research Council (Canada), CONICYT (Chile), Ministerio de Ciencia, Tecnologa e Innovacin Productiva (Argentina), and Ministrio da Ciłncia, Tecnologia e Inova£o (Brazil).

The Very Large Telescope is a facility of the European Organisation for Astronomical Research in the Southern Hemisphere. Our observations were carried out under ESO programme 089.C-0565 (PI Carry).

The Starfire Optical Range is owned and operated by the Air Force Research Laboratory, Directed Energy Directorate, on Kirtland AFB near Albuquerque, New Mexico. We acknowledge their support, especially from the observing staff at this facility. This paper is approved for public release; distribution is unlimited. Public Affairs release approval is AFRL-2020-0273.

This work was supported, in part, by research grants to our group (Merline PI) from the NASA Planetary Astronomy Program and the NSF Planetary Astronomy Program.

This research made use of NASA's Astrophysics Data System and JPL's Horizons ephemerides tool.

We thank Jerome Berthier and another anonymous reviewer for their careful reading of this manuscript, and for providing many helpful comments.

Appendix A. Triaxial ellipsoid radii, areas, and volumes

A.1. Triaxial Ellipsoid Lightcurves

The square of a Fourier expansion of a triaxial ellipsoid ($a > b > c$) lightcurve, where the intensity is proportional to the projected area (dropping factors of π), is

$$I^2 = (ac)^2 cos^2\theta cos^2\psi + (bc)^2 cos^2\theta sin^2\psi + (ab)^2 sin^2\theta \tag{A1}$$

where the sub-Earth latitude is θ and ψ is the rotational phase, with ψ=0 at maximum. (Included in the ψ's are longitude differences that convert synodic to sidereal rotations, described in the appendix of Drummond et al. (2016).) If we assume that Olympias' orbit also defines the asteroid's equatorial plane, that is, Roxane's spin pole is the same as the Olympias orbital pole, and since observations of Roxane and Olympias are always confined to within a few degrees of the satellite's orbital plane, we can assume the sub-Earth latitude on Roxane is always near θ=0. Setting θ to zero, and using trigonometric identities we can change Eq. (A1) to

$$I^2 = M + Ccos2\psi + Dsin2\psi \tag{A2}$$

where the mean brightness squared is $M = [(ac)^2 + (bc)^2]/2$ at $\psi = 45°$. The semi-amplitude is $\sqrt{C^2 + D^2} = \left[(ac)^2 - (bc)^2\right]\Big/2$. Thus,

$$a^2\Big/b^2 = \frac{M + \sqrt{C^2 + D^2}}{M - \sqrt{C^2 + D^2}} \quad . \tag{A3}$$

A.2. Brightness ratios

The square of the ratio or quotient (Q) of the brightness of Roxane and Olympias, both expressed with Eqs. (A1) or (A2), can also be fit for coefficients s as a Fourier series,

$$Q^2 = s_1 + s_2 cos2\psi_R + s_3 sin2\psi_R + s_4 cos2\psi_O + s_5 sin2\psi_O \tag{A4}$$

where the subscripts R and O refer to Roxane or Olympias, respectively. The semi-amplitude for Roxane is contained in coefficients s_2 and s_3, and for Olympias in s_4 and s_5. While the rotational period is known for Roxane, $P = 8.16961 \pm 0.00005$ h (Hanuš et al. 2016), where the error is from the Small

Bodies Data Ferret web site[5], Olympias' period is not. Therefore, we fix this period for Roxane (but not its amplitude) and search for the satellite period between 2 and 360 h that yielded the lowest residuals in a fit of Eq. (A4) with the magnitude differences from Tables B.18-B.21. Of the many periods producing local minima in residuals, we adopt the period for the smallest residuals, 8.2587±0.0001 h, and show the fits for both Roxane and Olympias in Fig. A.9.

Since our use of Eq. (A4) does not treat Olympias' period as an unknown, the error on Olympias' period is found by subtracting the contribution of Roxane from the best fit of Eq. (A4) and recasting the satellite data as a simple cosine function of time, where t includes the longitude differences in the previous *sec*tion

$$Q^2 - (s_1 + s_2 cos2\psi_R + s_3 sin2\psi_R) = Acos(2(t_O - t_z)2\pi/P) \quad . \tag{A5}$$

The new constants in this equation are A, the semi-amplitude of the satellite, t_z, the lightcurve zero point for the satellite, and P, its period, and their errors can be found from the covariance of the fit.

Let $q^2{=}s_1$ now denote the mean brightness ratio squared between Roxane and Olympias, and $A_R = \sqrt{s_2^2 + s_3^2}$ and $A_O = \sqrt{s_4^2 + s_5^2}$ refer to the semi-amplitude of brightness variation in the equatorial plane of Roxane and Olympias, respectively. The effective diameter for Roxane from Table 4 of 17.84 km, or an area of $r_e^2 = 9.58^2$ km^2, must come from the sum of the mean areas projected by Roxane and Olympias in Roxane's equatorial plane (Section 3.2),

$$r_e^2 = r_R^2 + r_O^2 = \sqrt{M_R} + \sqrt{M_O} = 9.58^2 \tag{A6}$$

while the ratio of the mean brightness of each is given by the first term in a fit of Eq. (A4) to brightness ratios,

$$r_R^2 \Big/ r_O^2 = \sqrt{M_R/M_O} = \sqrt{s_1} = q = 13.71 \tag{A7}$$

These two equations in two unknowns (r_R^2 and r_O^2) yield the mean area of each in its equatorial plane,

$$r_R^2 = \sqrt{\left((ac)_R^2 + (bc)_R^2\right)/2} = 9.58^2 \; q \Big/ (q+1) \quad ; \quad r_O^2 = \sqrt{\left((ac)_O^2 + (bc)_O^2\right)/2} = 9.58^2 \Big/ (q+1) \quad . \tag{A8}$$

We can normalize Eq. (A4) so that the first term becomes the mean of the brightness squared for an object by multiplying by either r_R^4 or r_O^4, dividing by $s_1 = q^2$, and taking the square root. Thus, the individual lightcurves can be extracted, with maxima of

$$(ac)_R = \frac{r_R^2\sqrt{q^2 + A_R}}{q} = \frac{9.58^2 q\sqrt{q^2 + A_R}}{q(q+1)} \quad ; \quad (ac)_O = \frac{r_O^2\sqrt{q^2 + A_O}}{q} = \frac{9.58^2\sqrt{q^2 + A_O}}{q(q+1)} \tag{A9}$$

and minima of

$$(bc)_R = \frac{r_R^2\sqrt{q^2 - A_R}}{q} = \frac{9.58^2 q\sqrt{q^2 - A_R}}{q(q+1)} \quad ; \quad (ac)_O = \frac{r_O^2\sqrt{q^2 - A_O}}{q} = \frac{9.58^2\sqrt{q^2 - A_O}}{q(q+1)} \quad . \tag{A10}$$

Table A.12 shows the values of quantities derived by combining the diameter of Roxane in Table 4 with the coefficients of a least squares fit of Eq. (A4) from our observations of the brightness ratios of Roxane to Olympias. The uncertainties in the table are propagated from the error of the mean of the diameter and the uncertainties in the coefficients.

Table A12
Projected Equatorial Areas (km^2) from Eqs. (A8)–(A10).

Area (km^2)	Roxane	Olympias
max: ac	104.5±6.0	7.29±0.41
mean: $c\sqrt{\left(a^2 + b^2\right)/2}$	85.5±3.6	6.24±0.26
min: bc	61.0±6.0	4.96±0.39
a/b	1.71±0.19	1.47±0.14

A.3. Triaxial ellipsoids

Since it is not possible to find a polar dimension c or axial ratios a/c or b/c from disk integrated measurements restricted to the equatorial plane, we estimate b/c in order to calculate individual volumes, and sum to obtain the total volume in the system. A hard lower limit to b/c is provided by a prolate spheroid, b/c=1. A soft upper limit is provided by assuming a hydrostatic equilibrium asteroid, as for liquid, sand or a rubble pile (Chandrasekhar 1969; Magnusson 1986; Magnusson et al. 1989; Drummond et al. 1988). We adopt the mean, b/c=1.18 for Roxane and 1.22 for Olympias, as depicted in Fig. A.10. This allows us to estimate c and b with Eq A10, and a with Eq A9

$$c = \sqrt{(bc)/(b/c)} \quad ; \quad b = bc \Big/ c \quad ; \quad a = ac \Big/ c \quad . \tag{A11}$$

Table A.13 gives the range of the triaxial ellipsoid axial radii.

[5] http://sbn.psi.edu/ferret/.

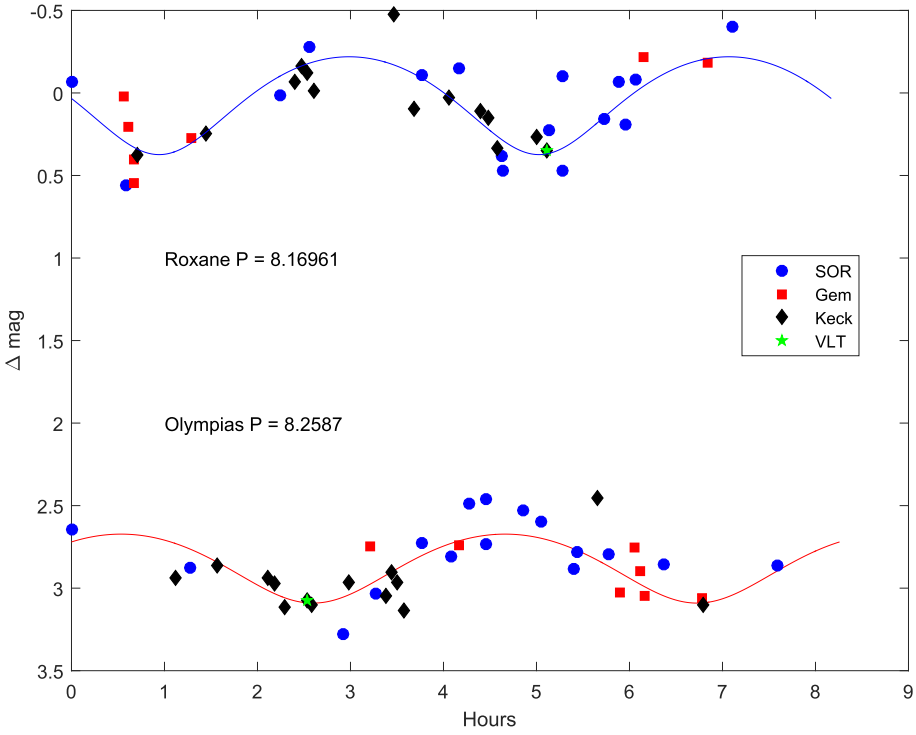

Fig. A.9. Lightcurves of Roxane and Olympias derived from their relative brightness. The hour zero-point is for the first SOR observation, and since the two periods are different, the two lightcurves will shift with respect to each other over time. The amplitude for Roxane is 0.58 magnitudes and 0.42 for Olympias.

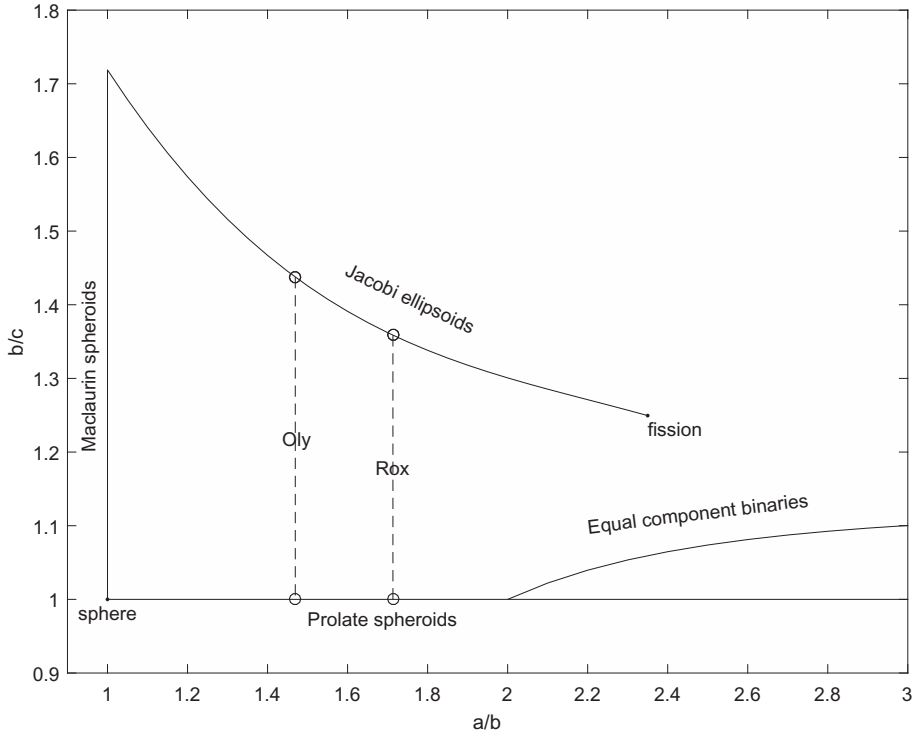

Fig. A.10. b/c as a function of a/b for hydrostatic equilibrium objects. The a/b values of Roxane and Olympias are from the brightness ratio lightcurves, with two values for each (circles), along the prolate spheroid line (a hard lower limit) and the equilibrium line (a soft upper limit). The adopted b/c values are midway between the two. Figure adapted from Drummond et al. (1988).

Table A.13
Range of triaxial ellipsoid radii (km)

Roxane	Olympias
$13.4 \leq a \lesssim 15.6$	$3.3 \leq a \lesssim 3.9$
$7.8 \leq b \lesssim 9.1$	$2.2 \leq b \lesssim 2.7$
$7.8 \geq c \gtrsim 6.7$	$2.2 \geq c \gtrsim 1.9$

Appendix B. Roxane and Olympias tables

B.1. Roxane observation logs

For the Observation Logs, columns contain the Julian date, calendar date, and UTC for each epoch, followed by the Right Ascension and Declination (J2000), the distance between the Earth and Roxane in AU, Roxane's V magnitude from Horizons (https://ssd.jpl.nasa.gov/?horizons) which does not include any variation with rotation, the solar phase angle, and the scale in km/″. Multiplying the scale by the appropriate θ from Table 1 gives the last column, the theoretical resolution, rexels, in km for a given observation.

Table B.14
Gemini observation log for Roxane

JD	Date	UTC	RA(°)	Dec(°)	Earth (AU)	Roxane V	Phase(°)	km/″	rex (km)
2455159.90147	2009-Nov-24	9:37	41.2	+12.7	1.262	12.9	8.6	915	49
2455159.98026	2009-Nov-24	11:31	41.2	+12.7	1.262	12.9	8.6	915	49
2455159.98266	2009-Nov-24	11:34	41.2	+12.7	1.262	12.9	8.6	915	39
2455159.98479	2009-Nov-24	11:37	41.2	+12.7	1.262	12.9	8.6	915	29
2455160.01062	2009-Nov-24	12:14	41.2	+12.7	1.262	12.9	8.6	915	49
2455160.76677	2009-Nov-25	6:23	41.0	+12.7	1.267	12.9	9.1	919	50
2455160.89378	2009-Nov-25	9:26	41.0	+12.7	1.267	12.9	9.1	919	50
2455161.00595	2009-Nov-25	12:08	41.0	+12.7	1.267	12.9	9.1	919	50

Observations at Gemini were under proposals GN-2009B-C-7 and GN-2010A-C 7, with Merline as PI. A negative detection was made on 2010-Mar-2 because the separation was too small.

Table B.15
Keck observation log for Roxane.

JD	Date	UTC	RA(°)	Dec(°)	Earth (AU)	Roxane V	Phase(°)	km/″	rex (km)
2456104.02728	2012-Jun-25	12:39	331.3	−10.5	1.368	13.4	23.3	992	43
2456105.02333	2012-Jun-26	12:33	331.4	−10.5	1.359	13.4	23.0	985	42
2456105.02654	2012-Jun-26	12:38	331.4	−10.5	1.358	13.4	23.0	985	33
2456105.03085	2012-Jun-26	12:44	331.4	−10.5	1.358	13.4	23.0	985	26
2456106.01463	2012-Jun-27	12:21	331.4	−10.5	1.349	13.4	22.8	979	42
2456122.93236	2012-Jul-15	12:02	331.3	−10.7	1.202	12.9	16.6	871	37
2456124.00422	2012-Jul-15	12:06	331.3	−10.7	1.202	12.9	16.6	871	37
2456124.00682	2012-Jul-15	12:10	331.3	−10.7	1.202	12.9	16.6	871	30
2456124.00977	2012-Jul-15	12:14	331.3	−10.7	1.202	12.9	16.6	871	23
2456148.91494	2012-Aug-09	9:57	327.3	−12.5	1.091	12.2	4.0	792	34
2456150.93203	2012-Aug-11	10:22	326.9	−12.7	1.088	12.1	2.8	789	34
2456154.93223	2012-Aug-15	10:22	326.0	−13.1	1.085	11.9	0.5	787	34
2456155.92204	2012-Aug-16	10:08	325.7	−13.2	1.085	11.9	0.2	787	27

Observations at Keck were mostly under Merline PI, with some of the time being shared with NASA/New Horizons and/or Team Keck. Additional negative observations were made on 2009-Dec-3, 2010-Mar-3, in 2012 on June-22, July-14, Aug-10, and on 2015-Feb-2 (Grundy, PI), all because the separation was too small or the AO performance was less than optimal.

Table B.16
VLT observation log for Roxane.

JD	Date	UTC	RA(°)	Dec(°)	Earth (AU)	Roxane V	Phase(°)	km/″	rex (km)
2456126.86430	2012-Jul-18	8:44	331.0	−10.8	1.183	12.9	15.4	858	11
2456137.72841	2012-Jul-29	5:29	329.6	−11.5	1.125	12.6	10.1	816	11
2456161.73878	2012-Aug-22	5:44	324.4	−13.8	1.089	12.2	3.5	790	21

Observations at VLT were under proposal 89.C-0565, Carry as PI.

Table B.17
SOR Observation log for Roxane.

JD	Date	UTC	RA(°)	Dec(°)	Earth (AU)	Roxane V	Phase(°)	km/″	rex (km)
2457673.83809	2016-Oct-12	8:06	65.9	18.9	1.407	13.5	19.7	1020	33
2457702.79152	2016-Nov-10	6:59	61.3	17.7	1.259	12.8	6.6	913	30
2457702.86034	2016-Nov-10	8:38	61.3	17.6	1.259	12.8	6.6	913	30
2457702.94051	2016-Nov-10	10:33	61.3	17.6	1.258	12.8	6.5	912	30
2457706.74925	2016-Nov-14	5:58	60.3	17.4	1.253	12.7	4.5	909	30
2457706.76342	2016-Nov-14	6:18	60.3	17.4	1.253	12.7	4.5	909	30
2457706.79549	2016-Nov-14	7:05	60.3	17.4	1.253	12.7	4.5	909	30
2457707.72477	2016-Nov-15	5:23	60.0	17.4	1.252	12.6	4.0	908	30
2457707.75899	2016-Nov-15	6:12	60.0	17.4	1.252	12.6	4.0	908	30
2457707.77960	2016-Nov-15	6:42	60.0	17.4	1.252	12.6	3.9	908	30
2457708.77233	2016-Nov-16	6:31	59.8	17.3	1.252	12.6	3.4	908	30
2457708.79735	2016-Nov-16	7:07	59.8	17.3	1.252	12.6	3.4	908	30
2457708.77240	2016-Nov-16	6:31	59.8	17.3	1.252	12.6	3.4	908	15
2457710.78705	2016-Nov-18	6:52	59.2	17.2	1.252	12.5	2.4	908	30
2457710.80817	2016-Nov-18	7:23	59.2	17.2	1.252	12.5	2.4	908	30
2457779.64878	2017-Jan-26	3:33	52.8	16.8	1.796	14.2	23.9	1303	43
2457779.66001	2017-Jan-26	3:49	52.8	16.8	1.796	14.2	23.9	1303	43
2457785.58762	2017-Feb-01	2:05	53.8	17.2	1.873	14.4	24.5	1358	44
2457785.63832	2017-Feb-01	3:18	53.8	17.2	1.873	14.4	24.5	1358	44

Observations at the SOR were obtained by Reynolds or Buckman.

B.2. Olympias measurements

For the measurement tables, columns contain the UTC date and time, the position angle for Olympias with respect to Roxane, the separation between the two in km and arc seconds, and the measured magnitude difference between them. ΔMags marked with an asterisk were not used in the lightcurves in Fig. A.9. The standard astronomical filters employed are given under the Notes. The number of sets, the total number frames, and the total integration time for each epoch are given in the last three columns.

Table B.18
Measurements of Olympias at Gemini.

Date	UTC	PA(°)	Sep (km)	Sep (″)	Δ Mag	Notes	sets	frames	Tot exp (*sec*)
2009-Nov-24	9:37	76.2	255.5	0.279	3.12	K	1	12	60
2009-Nov-24	11:31	76.0	249.4	0.273	2.70	K	1	12	24
2009-Nov-24	11:34	75.6	242.5	0.265	2.43	H	1	12	36
2009-Nov-24	11:37	76.2	230.1	0.252	2.06	J	1	4	64
2009-Nov-24	12:14	76.1	243.9	0.267	2.07	K	1	12	96
2009-Nov-25	6:23	76.7	204.0	0.222	3.91*	K	1	12	24
2009-Nov-25	9:26	77.8	190.9	0.208	2.97	K	1	12	24
2009-Nov-25	12:08	77.2	188.4	0.205	2.10	K	1	12	120

Table B.19
Measurements of Olympias at Keck.

Date	UTC	PA(°)	Sep (km)	Sep (″)	Δ Mag	Notes	sets	frames	Tot exp (sec)
2012-Jun-25	12:39	75.0	202.5	0.204	2.19	K	1	9	90
2012-Jun-26	12:33	76.0	257.3	0.261	2.52	K	1	9	45
2012-Jun-26	12:38	76.0	254.6	0.258	2.42	H	1	9	36
2012-Jun-26	12:44	73.5	254.7	0.259	2.01	J	1	9	90
2012-Jun-27	12:21	75.3	252.5	0.258	2.88	K	1	9	45
2012-Jul-15	12:02	256.1	228.4	0.262	2.84	K	1	9	26.1
2012-Jul-15	12:06	256.4	227.9	0.262	2.96	K	1	9	4.5
2012-Jul-15	12:10	256.2	227.8	0.261	2.93	H	1	9	4.5
2012-Jul-15	12:14	256.3	226.9	0.260	2.84	J	1	9	9
2012-Aug-09	9:57	256.1	163.8	0.207	2.55	K	1	15	45
2012-Aug-11	10:22	80.6	91.8	0.116	3.32	K	3	8	3.8
2012-Aug-15	10:22	75.6	217.8	0.277	2.13	K	1	1	30
2012-Aug-16	10:08	84.6	104.2	0.132	2.47	H	1	7	35

Table B.20
Measurements of Olympias at VLT.

Date	UTC	PA(°)	Sep (km)	Sep (″)	Δ Mag	Notes	sets	frames	Tot exp (sec)
2012-Jul-18	8:44	74.2	95.1	0.111	4.35*	H WFOV	4	164	164
2012-Jul-29	5:29	247.6	60.4	0.074	1.86	H WFOV	4	84	168
2012-Aug-22	5:44	250.7	82.7	0.105	3.72*	H NFOV	6	92	248

Table B.21
Measurements of Olympias at SOR.

Date	UTC	PA(°)	Sep (km)	Sep (″)	Δ Mag	Notes	sets	frames	Tot exp (sec)
2016-Oct-12	8:06	258.3	259.6	0.254	3.02		2	11	111
2016-Nov-10	6:59	79.3	201.2	0.220	2.48		2	15	100
2016-Nov-10	8:38	79.3	218.2	0.239	2.61	Gs	3	17	36
2016-Nov-10	10:33	78.6	257.5	0.282	3.12		5	25	82
2016-Nov-14	5:58	256.7	104.6	0.115	2.78	Seq	3	26	62
2016-Nov-14	6:18	263.7	110.4	0.121	2.90	Seq	3	19	81
2016-Nov-14	7:05	260.8	83.1	0.091	2.52*	Seq	3	10	65
2016-Nov-15	5:23	255.9	181.0	0.199	2.61		4	24	84
2016-Nov-15	6:12	252.6	217.2	0.239	5.11*		2	8	25
2016-Nov-15	6:42	257.5	160.8	0.177	2.76		3	8	32
2016-Nov-16	6:31	258.5	256.6	0.283	3.08		3	22	52
2016-Nov-16	7:07	258.0	241.6	0.266	3.04		2	8	25
2016-Nov-16	6:31	257.8	262.9	0.290	2.70	RI	4	12	105
2016-Nov-18	6:52	248.9	147.5	0.162	2.19		8	24	154
2016-Nov-18	7:23	257.1	135.8	0.150	2.68		3	14	55
2017-Jan-26	3:33	250.3	151.3	0.116	3.32		3	11	115
2017-Jan-26	3:49	256.8	156.7	0.120	2.26*		3	18	74
2017-Feb-01	2:05	80.6	180.3	0.133	3.01		4	27	212
2017-Feb-01	3:18	79.9	188.9	0.139	2.91		7	48	318

Under Notes in this table for the SOR, Seq indicates a sequential fit of asteroid and then satellite (after subtracting asteroid), otherwise a simultaneous fit for both, RI indicates that the imaging wavelength was 0.81 μm, otherwise 1.23 μm (J-band), and Gs indicates that the fit was for Gaussians, not Lorentzians.

Appendix C. Kalliope and Linus tables

C.1. Kalliope Observation Log

Table C.22
SOR observation log for Kalliope.

JD	Date	UTC	RA(°)	Dec(°)	Earth (AU)	Kalliope V	Phase(°)	km/″
2457699.78384	2016-Nov-07	6:48	103.9	+28.6	1.971	10.9	18.4	1429
2457701.87100	2016-Nov-09	8:54	103.9	+28.8	1.949	10.9	18.0	1414
2457702.86555	2016-Nov-10	8:46	104.0	+28.9	1.939	10.8	17.7	1406
2457702.94318	2016-Nov-10	10:38	104.0	+28.9	1.938	10.8	17.7	1406
2457706.77814	2016-Nov-14	6:40	103.9	+29.3	1.900	10.8	16.8	1378
2457707.77745	2016-Nov-15	6:39	103.9	+29.4	1.891	10.8	16.5	1371
2457708.79945	2016-Nov-16	7:11	103.9	+29.5	1.881	10.7	16.2	1365
2457728.76039	2016-Dec-06	6:14	101.5	+31.9	1.737	10.4	9.7	1260
2457765.70594	2017-Jan-12	4:56	92.2	+35.1	1.742	10.4	8.3	1264
2457765.70667	2017-Jan-12	4:57	92.2	+35.1	1.742	10.3	8.3	1264
2457779.65292	2017-Jan-26	3:40	89.6	+35.5	1.840	10.6	13.1	1335
2457793.81231	2017-Feb-09	7:29	88.4	+35.5	1.969	10.9	16.7	1428
2457793.83441	2017-Feb-09	8:01	88.4	+35.5	1.969	10.9	16.7	1428
2457794.68842	2017-Feb-10	4:31	88.4	+35.5	1.990	10.9	17.2	1443
2457794.80110	2017-Feb-10	7:13	88.4	+35.5	1.991	10.9	17.2	1444
2457794.68934	2017-Feb-10	4:32	88.4	+35.5	1.990	10.9	17.2	1443
2457794.80182	2017-Feb-10	7:14	88.4	+35.5	1.991	10.9	17.2	1444

Columns contain the Julian date, calendar date, and UTC for each epoch, followed by the Right Ascension and Declination (J2000), the distance between the Earth and Kalliope in AU, Kalliope's V magnitude from Horizons (https://ssd.jpl.nasa.gov/?horizons) which does not include any variation with rotation, the solar phase angle, and the scale in km/″ at the asteroid.

C.2. Linus measurements

Table C.23
SOR measurements of Linus.

Date	UTC	PA(°)	Sep (km)	Sep (″)	Δ Mag	Notes	sets	frames	Tot exp (sec)
2016-Nov-07	6:48	184.9	977	0.684	3.45		2	22	76
2016-Nov-09	8:54	5.1	611	0.432	3.46		2	13	140
2016-Nov-10	8:46	182.1	1040	0.740	3.43		3	17	109
2016-Nov-10	10:38	182.8	1063	0.756	2.70		2	6	40
2016-Nov-14	6:40	183.7	1070	0.776	3.40		3	12	60
2016-Nov-15	6:39	352.2	358	0.261	2.95	Seq	3	20	40
2016-Nov-16	7:11	4.1	943	0.691	2.74		3	10	45
2016-Dec-06	6:14	188.1	713	0.565	3.74		1	10	50
2017-Jan-12	4:56	350.2	1041	0.824	2.88		1	20	100
2017-Jan-12	4:57	350.6	986	0.780	3.64	RI	1	20	100
2017-Jan-26	3:40	322.3	492	0.369	3.61	Seq	2	7	45
2017-Feb-09	7:29	254.7	278	0.194	2.98	Seq	3	60	61
2017-Feb-09	8:01	266.5	286	0.200	4.06	Seq	4	70	250
2017-Feb-10	4:31	353.7	1092	0.757	2.68		3	84	395

(continued on next page)

Table C.23 (*continued*)

Date	UTC	PA(°)	Sep (km)	Sep (″)	Δ Mag	Notes	sets	frames	Tot exp (sec)
2017-Feb-10	7:13	356.7	1083	0.750	3.20		4	70	376
2017-Feb-10	4:32	354.2	1074	0.744	2.94	RI	3	63	735
2017-Feb-10	7:14	357.1	1040	0.721	3.26	RI	4	78	760

Columns contain the UTC date and time, the position angle for Linus with respect to Kalliope, the separation between the two in km and arc seconds, and the measured magnitude difference between them. Under Notes, Seq indicates a sequential fit of asteroid and then moon (after subtracting asteroid), otherwise a simultaneous fit for both, and RI indicates that the imaging wavelength was 0.81 μm, otherwise 1.23 μm (J-band). The number of sets, the total number frames, and the total integration time for each epoch are given in the last three columns.

References

Alí-Lagoa, V., Müller, T.G., Usui, F., Hasegawa, S., 2018. The AKARI IRC asteroid flux catalogue: updated diameters and albedos. Astron. Astrophys. 612.

Archinal, B.A., et al., 2018. Report of the IAU Working Group on Cartographic Coordinates and Rotational Elements: 2015. Celestial Mechanics and Dynamical Astronomy 130, 22.

Bevington, P. R., Robinson, D. K. 2003. Data Reduction and Error Analysis for the Physical Sciences, 3rd ed., by Philip R. Bevington and Keith D. Robinson. Boston, MA: McGraw-Hill, ISBN 0-07-247227-8.

Carry, B., 2012. Density of asteroids. Planet. Space Sci. 73, 98–118.

Chandrasekhar, S., 1969. Ellipsoidal figures of equilibrium. In: The Silliman Foundation Lectures. Yale University Press, New Haven, p. 1969.

Ćuk, M., Burns, J.A., 2005. Effects of thermal radiation on the dynamics of binary NEAs. Icarus 176, 418.

van Dam, M.A., Le Mignant, D., Macintosh, B.A., 2004. Performance of the Keck Observatory Adaptive-Optics System. Applied Optics 43, 5458.

DeMeo, F.E., et al., 2011. A spectral comparison of (379) Huenna and its satellite. Icarus 212, 677.

Descamps, P., et al., 2008. New determination of the size and bulk density of the binary Asteroid 22 Kalliope from observations of mutual eclipses. Icarus 196, 578–600.

Drummond, J.D., 1998. Adaptive optics Lorentzian point spread function. In: Adaptive Optical System Technologies, SPIE 3353, pp. 1030–1037.

Drummond, J.D., 2014. Binary Stars Observed with Adaptive Optics at the starfire Optical Range. The Astronomical Journal 147, 65.

Drummond, J.D., Weidenschilling, S.J., Chapman, C.R., Davis, D.R., 1988. Photometric geodesy of main-belt asteroids. II - Analysis of lightcurves for poles, periods, and shapes. Icarus 76, 19–77.

Drummond, J.D., Reynolds, O.R., Buckman, M.D., 2016. The orbit and size of (87) Sylvia's Romulus from the 2015 apparition. Icarus 276, 107–115.

Drummond, J.D., Reynolds, O., Buckman, M., Eickhoff, M., 2017. The orbits of satellites of (22) Kalliope and (317) Roxane. AAS/Division for Planetary Sciences Meeting Abstracts #49 49, 110.30.

Durda, D.D., et al., 2004a. The formation of asteroid satellites in large impacts: results from numerical simulations. Icarus 170, 243.

Durda, D.D., et al., 2004b. Erratum to "The formation of asteroid satellites in large impacts: results from numerical simulations"[Icarus 167 (2004) 382-396]. Icarus 170, 242.

Durda, D.D., Enke, B.L., Merline, W.J., Richardson, D.C., Asphaug, E., Bottke, W.F., 2010. Comparing the Properties of Observed Main-Belt Asteroid Binaries and Modeled Escaping Ejecta Binaries (EEBs) from Numerical Simulations. Lunar and Planetary Science Conference 2558.

Ďurech, J., et al., 2011. Combining asteroid models derived by lightcurve inversion with asteroidal occultation silhouettes. Icarus 214, 652–670.

Ďurech, J., Sidorin, V., Kaasalainen, M., 2010. DAMIT: a database of asteroid models. Astronomy and Astrophysics 513, A46.

Fienga, A., Manche, H., Laskar, J., Gastineau, M., Verma, A., 2013. INPOP new release: INPOP10e. ArXiv e-prints.

Fienga, A., Avdellidou, C., Hanuš, J., 2020. Asteroid masses obtained with INPOP planetary ephemerides. Monthly Not. R. Astronom. Soc. 492, 589–602.

Folkner, W.M., Williams, J.G., Boggs, D.H., 2009. The planetary and lunar ephemeris de 421. IPN Prog. Rep. 42, 1–34.

Goffin, E., 2014. Astrometric asteroid masses: a simultaneous determination. Astron. Astrophys. 565, A56.

Green, D.W.E., 2001. S/2001 (22) 1. Int. Astron. Union Circ. 7703, 1.

Hanuš, J., et al., 2013a. An anisotropic distribution of spin vectors in asteroid families. Astron. Astrophys. 559, A134.

Hanuš, J., et al., 2016. New and updated convex shape models of asteroids based on optical data from a large collaboration network. Astron. Astrophys. 586.

Hanuš, J., et al., 2017. Volumes and bulk densities of forty asteroids from ADAM shape modeling. Astron. Astrophys. 601, A114.

Hanuš, J., Marchis, F., Ďurech, J., 2013b. Sizes of main-belt asteroids by combining shape models and Keck adaptive optics observations. Icarus 226, 1045–1057.

Herald, D., et al., 2019. Asteroid Occultations V3.0. NASA Planetary Data System, Asteroid Occultations V3.0. urn:nasa:pds:smallbodiesoccultations::3.0.

Herriot, G., et al., 2000. Progress on Altair: the Gemini North adaptive optics system. Adapt. Opt. Syst. Technol. 115.

Hodapp, K.W., et al., 2003. The Gemini Near-Infrared Imager (NIRI). In: Publications of the Astronomical Society of the Pacific, 115, p. 1388.

Jacobson, S.A., Scheeres, D.J., McMahon, J., 2014. Formation of the Wide Asynchronous Binary Asteroid Population. Astrophys. J. 780, 60.

Kochetova, O.M., 2004. Determination of large asteroid masses by the dynamical method. Solar Syst. Res. 38, 66–75.

Lenzen, R., et al., 2003. NAOS-CONICA first on sky results in a variety of observing modes. Instrument Design and Performance for Optical/infrared Ground-based Telescopes, p. 944.

Magnusson, P., 1986. Distribution of spin axes and senses of rotation for 20 large asteroids. Icarus 68, 1–39.

Magnusson, P., Barucci, M.A., Drummond, J.D., Lumme, K., Ostro, S.J., 1989. Determination of pole orientations and shapes of asteroids. Asteroids II 67–97.

Magri, C., Nolan, M.C., Ostro, S.J., Giorgini, J.D., 2007. A radar survey of main-belt asteroids: Arecibo observations of 55 objects during 1999-2003. Icarus 186, 126–151.

Marchis, F., et al., 2003. A three-dimensional solution for the orbit of the asteroidal satellite of 22 Kalliope. Icarus 165, 112–120.

Marchis, F., et al., 2008. Main belt binary asteroidal systems with circular mutual orbits. Icarus 196 (1), 97–118.

Marchis, F., et al., 2012. Multiple asteroid systems: Dimensions and thermal properties from spitzer space telescope and ground-based observations. Icarus 221, 1130–1161.

Margot, J.L., Brown, M.E., 2001a. S/2001 (22) 1. International Astronomical Union Circular 7703, p. 3.

Margot, J.L., Brown, M.E., 2001b. Discovery and characterization of binary asteroids 22 Kalliope and 87 Sylvia. Bull. Am. Astron. Soc. 33, 52.02.

Margot, J.L., Brown, M.E., 2003. A Low-Density M-type Asteroid in the Main Belt. Science 300, 1939–1942.

Masiero, J.R., et al., 2011. Main belt asteroids with WISE/NEOWISE. I. Preliminary albedos and diameters. Astrophys. J. 741, 68.

Masiero, J.R., et al., 2012. Preliminary analysis of WISE/NEOWISE 3-band cryogenic and post-cryogenic observations of main belt asteroids. Astrophys. J. 759, L8.

Masiero, J.R., et al., 2014. Main-belt Asteroids with WISE/NEOWISE: Near-infrared Albedos. Astrophys. J. 791, 121.

Merline, W.J., et al., 1999. Discovery of a moon orbiting the asteroid 45 Eugenia. Nature 401, 565. https://doi.org/10.1038/44089.

Merline, W.J., et al., 1999a. Discovery of Asteroidal Satellite S/1998 (45) 1. AAS/Division for Planetary Sciences Meeting Abstracts #31.

Merline, W.J., Menard, F., Close, L., Dumas, C., Chapman, C.R., Slater, D.C., 2001a. S/2001 (22) 1. International Astronomical Union Circular 7703, p. 2.

Merline, W.J., Close, L.M., Menard, F., Dumas, C., Chapman, C.R., Slater, D.C., 2001b. Search for asteroid satellites. Bull. Am. Astron. Soc. 33, 52.01.

Merline, W.J., Weidenschilling, S.J., Durda, D.D., Margot, J.L., Pravec, P., Storrs, A.D., 2002. Asteroids do have satellites. Asteroids III 289–312.

Merline, W.J., Tamblyn, P.M., Drummond, J.D., Christou, J.C., Conrad, A.R., Carry, B., Chapman, C.R., Dumas, C., Durda, D.D., Owen, W.M., Enke, B.L., 2009. S/2009 (317) 1. International Astronomical Union Circular 9099, p. 2.

Milli, J., 16 colleagues 2018, 2018. Low wind effect on VLT/SPHERE: impact, mitigation strategy, and results. Adaptive Optics Systems VI 10703. https://doi.org/10.1117/12.2311499.

Morrison, D., Zellner, B., 2007. TRIAD Radiometric Diameters and Albedos. NASA Planetary Data System, EAR-A-COMPIL-5-TRIADRAD-V1.0.

N'Diaye, M., et al., 2018. Calibration of the island effect: experimental validation of closed-loop focal plane wavefront control on Subaru/SCExAO. Astron. Astrophys. 610, A18.

Polishook, D., 2012. Studying spin axis of primary components of binary asteroids and asteroid pairs. Asteroids, Comets, Meteors 2012, 6487.

Polishook, D., Brosch, N., Prialnik, D., Kaspi, S., 2009. Simultaneous spectroscopic and photometric observations of binary asteroids. Meteorit. Planet. Sci. 44, 1955.

Polishook, D., Brosch, N., Prialnik, D., 2011. Rotation periods of binary asteroids with large separations - Confronting the Escaping Ejecta Binaries model with observations. Icarus 212, 167.

Pravec, P., et al., 2010. Formation of asteroid pairs by rotational fission. Nature 466, 1085.

Pravec, P., Harris, A.W., Kušnirák, P., Galád, A., Hornoch, K., 2012. Absolute magnitudes of asteroids and a revision of asteroid albedo estimates from WISE thermal observations. Icarus 221, 365.

Rousset, G., et al., 2003. NAOS, the first AO system of the VLT: on-sky performance. In: Adaptive Optical System Technologies II 140.

Ryan, E.L., Woodward, C.E., 2010. Rectified asteroid albedos and diameters from IRAS and MSX photometry catalogs. Astron. Astrophys. 140, 933–943.

Sauvage, J.-F., et al., 2016. Tackling down the low wind effect on SPHERE instrument. Adapt. Optics Syst. V 9909, 990916.

Scheeres, D.J., 2007. The dynamical evolution of uniformly rotating asteroids subject to YORP. Icarus 188, 430.

Tedesco, E.F., Noah, P.V., Noah, M.C., Price, S.D., 2004. IRAS Minor Planet Survey. NASA Planetary Data System, IRAS-A-FPA-3-RDR-IMPS-V6.0.
Usui, F., et al., 2013. Albedo properties of main belt asteroids based on the all-sky survey of the infrared astronomical satellite AKARI. Astrophys. J. 762. https://doi.org/10.1088/0004-637X/762/1/56.
Vachier, F., Berthier, J., Marchis, F., 2012. Determination of binary asteroid orbits with a genetic-based algorithm. Astron. Astrophys. 543, A68.
Vigan, A., 9 colleagues 2018, 2018. On-sky compensation of non-common path aberrations with the ZELDA wavefront sensor in VLT/SPHERE. Adaptive Optics Systems VI 10703. https://doi.org/10.1117/12.2313656.
Viswanathan, V., Fienga, A., Gastineau, M., Laskar, J., 2017. INPOP17a planetary ephemerides. Notes Scientifiques et Techniques de l'Institut de mécanique céleste, (ISSN 1621-3823), #108. ISBN 2-910015-79-3, 2017, 39 pp. 108.
Walsh, K.J., Jacobson, S.A., 2015. Formation and evolution of binary asteroids. Asteroids IV 375.
Walsh, K.J., Richardson, D.C., Michel, P., 2008. Rotational breakup as the origin of small binary asteroids. Nature 454, 188.
Wilby, M.J., et al., 2018. Laboratory verification of Fast & Furious phase diversity: Towards controlling the low wind effect in the SPHERE instrument. Astron. Astrophys. 615, A34.
Wizinowich, P.L., et al., 2004. Adaptive optics developments at Keck Observatory. Advan. Adapt. Opt. 1.
Yang, B., et al., 2016. Extreme AO observations of two triple asteroid systems with SPHERE. Astrophys. J. 820, L35.
Zielenbach, W., 2011. Mass determination studies of 104 large asteroids. Astron. Astrophys. 142, 120–128.